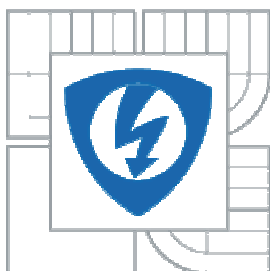




VYSOKÉ UČENÍ TECHNICKÉ V BRNĚ  
BRNO UNIVERSITY OF TECHNOLOGY



FAKULTA ELEKTROTECHNIKY A KOMUNIKAČNÍCH  
TECHNOLOGIÍ  
ÚSTAV RADIOELEKTRONIKY

FACULTY OF ELECTRICAL ENGINEERING AND COMMUNICATION  
DEPARTMENT OF RADIO ELECTRONIC

## (SUB)MILLIMETER-WAVE ANTENNAS

ANTÉNY PRO PÁSMO (SUB)MILIMETROVÝCH VLN

DOKTORSKÁ PRÁCE

DOCTORAL THESIS

**AUTOR PRÁCE**

AUTHOR

**KAMIL PÍTRA**

**VEDOUcí PRÁCE**

SUPERVISORS

**Prof. ZBYNĚK RAIDA**

**Prof. HANS LUDWIG HARTNAGEL**

BRNO 2014

## **ABSTRACT**

The thesis deals with the design and optimization of circularly polarized antennas for THz frequencies. In the thesis, a simplified theory of THz sources is presented, and a suitable antenna for a THz source is designed. The design is focused on achieving circular polarization from linearly polarized antennas. In order to suppress surface waves on an electrically dense dielectric substrate, we design and optimize specific periodic structures. The design of such a structure is rather complicated since the relation between electromagnetic band gap (EBG) properties and unit cell geometry is not straightforward. In order to properly focus the radiated energy, we design and optimize a partially reflective surface (PRS) acting as a planar lens for the THz antenna.

## **KEYWORDS**

THz antenna, THz source, dual-slot antenna, electromagnetic band gap structure (EBG), mushroom-like EBG, partially reflective surface (PRS), planar lens.

## **ABSTRAKT**

Disertační práce se zabývá návrhem a optimalizací kruhově polarizované antény pro oblast terahertzových kmitočtů. V práci se věnují zjednodušené teorii terahertzového zdroje a návrhu vhodné antény pro tento zdroj. Návrh je zaměřen na dosažení kruhové polarizace z lineárně polarizovaných antén. Abych potlačil šíření povrchové vlny na elektricky tlustém dielektrickém substrátu, věnuji se návrhu a optimalizaci specifických periodických struktur. Návrh těchto struktur je poměrně komplikovaný, protože neexistuje přímočarý vztah mezi vlastnostmi struktur s elektromagnetickým zádržným pásmem (EBG) a geometrií buňky. Abych vhodně koncentroval vyzařovanou energii do úzkého svazku, věnuji se návrhu a optimalizaci částečně odrazné plochy (PRS), které působí jako planární čočka pro terahertzovou anténu.

## **KLÍČOVÁ SLOVA**

Terahertzová anténa, terahertzový zdroj, dvojštěrbinová anténa, struktura s elektromagnetickým zádržným pásmem (EBG), hříbková EBG struktura, částečně odrazný povrch (PRS), planární čočka.

## DECLARATION

I declare that I have written my doctoral thesis “(Sub)millimeter-wave antennas” independently, under the guidance of the doctoral thesis supervisor and using the technical literature and other sources of information which are all quoted in the thesis and detailed in the list of literature at the end of the thesis.

As the author of the doctoral thesis, I furthermore declare that, as regards the creation of this doctoral thesis, I have not infringed any copyright. In particular, I have not unlawfully encroached on anyone’s personal and/or ownership rights and I am fully aware of the consequences in the case of breaking Regulation §11 and the following of the Copyright Act No. 121/2000 Coll., and of the rights related to intellectual property right and changes in some Acts (Intellectual Property Act) and formulated in later regulations, inclusive of the possible consequences resulting from the provisions of Criminal Act No. 40/2009 Coll., Section 2, Head VI, Part 4.

Brno, the 6<sup>th</sup> of January, 2014

---

Kamil Pítra

## BIBLIOGRAPHIC CITATION

PÍTRA, K. *(Sub)millimeter-wave antennas*. Doctoral dissertation thesis. Brno: Brno University of Technology, Faculty of Electrical Engineering and Communication, 2014.

PÍTRA, K. *Antény pro pásmo (sub)milimetrových vln*. Doktorská disertační práce. Brno: Vysoké učení technické v Brně, Fakulta elektrotechniky a komunikačních technologií, 2014.

## ACKNOWLEDGEMENT

I would like to express my gratitude to my supervisor Prof. Dr. Eng. Dr. h.c. mult. Hans Ludwig Hartnagel for giving me an opportunity to work with him and for his advice and invaluable guidance throughout my research. Gratitude is also due to Prof. Dr. Ing. Zbyněk Raida for his advice and invaluable guidance throughout my research. I would like to thank M.Sc Shihab Al-Daffaie for perfect discussion and new ideas. This thesis would have been impossible without their precious ideas and support. Last but not least, I would like to thank my girlfriend Petra Kolářková for her patience and giving me the motivation to finish my studies

Brno, the 6<sup>th</sup> of January, 2014

---

Kamil Pítra



The research described in my thesis was performed in laboratories of the SIX Research Center, the registration number CZ.1.05/2.1.00/03.0072, the operational program Research and Development for Innovation.

# CONTENTS

|          |   |           |
|----------|---|-----------|
| <b>1</b> | <b>INTRODUCTION .....</b>                                 | <b>12</b> |
| <b>2</b> | <b>STATE-OF-THE-ART .....</b>                             | <b>14</b> |
| 2.1      | ANTENNAS FOR INTEGRATED PHOTOMIXERS .....                 | 14        |
| <b>3</b> | <b>OBJECTIVES .....</b>                                   | <b>16</b> |
| <b>4</b> | <b>NOVEL MULTI-LAYER THZ SOURCE .....</b>                 | <b>17</b> |
| 4.1      | CIRCULAR POLARIZATION .....                               | 17        |
| 4.2      | OPERATING PRINCIPLE .....                                 | 17        |
| <b>5</b> | <b>THZ SOURCE AND THZ CP ANTENNA .....</b>                | <b>19</b> |
| 5.1      | PHOTOMIXING .....   | 19        |
| 5.2      | PHOTOCONDUCTIVE MIXERS .....                              | 20        |
| 5.3      | THZ SOURCE OVERVIEW .....                                 | 21        |
| 5.4      | DUAL-SLOT ANTENNA LIKE THZ SOURCE .....                   | 22        |
| 5.5      | FOUR-LEAF-CLOVER-SHAPED DIPOLE LIKE THZ SOURCE .....      | 26        |
| 5.6      | THE CP THZ CROSS-SLOT PATCH ANTENNA .....                 | 28        |
| 5.7      | SUMMARY .....   | 31        |
| <b>6</b> | <b>PERIODIC STRUCTURES AND PLANAR LENS .....</b>          | <b>33</b> |
| 6.1      | OVERVIEW OF METALLO-DIELECTRIC PERIODIC STRUCTURES .....  | 33        |
| 6.2      | SURFACE WAVES .....                                       | 34        |
| 6.3      | ANALYSIS AND DESIGN OF MUSHROOM-LIKE EBG STRUCTURES ..... | 35        |
| 6.4      | VERIFICATION OF THE DESIGN METHOD .....                   | 39        |
| 6.5      | THZ MUSHROOM-LIKE EBG STRUCTURE .....                     | 42        |
| 6.6      | THZ SUPERSTRATES .....                                    | 47        |
| 6.7      | THZ PLANAR LENSES .....                                   | 49        |
| 6.8      | REDUCING HEIGHT OF RESONANT CAVITY .....                  | 52        |
| 6.9      | THZ LC SUPERSTRATE LIKE PLANAR LENS .....                 | 53        |
| 6.10     | SUMMARY .....   | 58        |
| <b>7</b> | <b>FINAL THZ ANTENNA .....</b>                            | <b>59</b> |
| 7.1      | CIRCULARLY POLARIZED THZ ANTENNA .....                    | 59        |
| 7.2      | FABRICATION AND TECHNOLOGY ASPECTS .....                  | 62        |
| 7.3      | EXPERIMENTAL VERIFICATION AT $F = 10$ GHz .....           | 63        |
| <b>8</b> | <b>CONCLUSION .....</b>                                   | <b>68</b> |
|          | <b>REFERENCES .....</b>                                   | <b>70</b> |
|          | <b>CURRICULUM VITAE .....</b>                             | <b>74</b> |

## LIST OF FIGURES

|   |    |
|---|----|
| Fig. 1.1: Electromagnetic spectrum from radio frequency (RF) to ultra-violet (UV) . . .                       | 12 |
| Fig. 4.1: Sketch of the proposed THz source.....  | 17 |
| Fig. 5.1: Basic principle of photomixing. ....  | 19 |
| Fig. 5.2: LT-GaAs photomixer. ....  | 20 |
| Fig. 5.3: Equivalent-circuit model of the photomixer antenna. ....  | 21 |
| Fig. 5.4: CST model of an IDE photomixer and equivalent capacitor $\pi$ -network.....                         | 23 |
| Fig. 5.5: Test capacitor: $W_f = 1\mu\text{m}$ , $L_f = 9\mu\text{m}$ , $W_g = 1\mu\text{m}$ , $N = 6$ . .... | 23 |
| Fig. 5.6: The coordination system of the proposed antenna. ....   | 24 |
| Fig. 5.7: Designed dual-slot antenna. ....  | 24 |
| Fig. 5.8: RF choke filter without dipole arms.....  | 25 |
| Fig. 5.9: Radiation patterns of the dual-slot antenna like THz source.....                                    | 26 |
| Fig. 5.8: Frequency response of axial ratio for different feeding techniques. ....                            | 26 |
| Fig. 5.9: The designed four-leaf-clover-shaped dipole antenna and biasing scheme. ....                        | 27 |
| Fig. 5.10: Input resistance of the designed antenna.....  | 27 |
| Fig 5.11: Radiation patterns of the four-leaf-clover-shaped dipole antenna like THz source. ....              | 28 |
| Fig. 5.12: Principle of creating circularly polarized wave.....   | 29 |
| Fig. 5.13: Geometry of the designed antenna. ....   | 29 |
| Fig. 5.14: Radiation pattern of the CP THz cross-slot patch antenna, a) XZ plane, b) YZ plane.....            | 30 |
| Fig. 5.15: Axial ratio in broadside direction of the CP THz cross-slot patch antenna. ..                      | 30 |
| Fig. 5.16: Equivalent circuit model of the designed antenna.....  | 31 |
| Fig. 6.1: Metallo-dielectric periodic structures.....   | 33 |
| Fig. 6.2: Propagation of surface waves inside the grounded dielectric substrate. ....                         | 34 |
| Fig. 6.3: Configuration of the mushroom-like EBG structure.....   | 35 |
| Fig. 6.4: LC equivalent circuit of the mushroom-like EBG structure. ....                                      | 36 |
| Fig. 6.5: The imaginary part of the surface impedance. ....   | 36 |
| Fig. 6.6: Reflection phase calculated from LC equivalent circuit. ....  | 37 |
| Fig. 6.7: The irreducible Brillouin zone [44].....  | 38 |
| Fig. 6.8: Dispersion diagram of the mushroom-like EBG structure. ....   | 38 |
| Fig. 6.9: The dimensions of the unit cell. ....   | 39 |

|  |    |
|--|----|
| Fig. 6.10: Reflection phase response of the mushroom-like EBG structure.....   | 39 |
| Fig. 6.11: Dispersion diagram of the mushroom-like EBG structure.....  | 40 |
| Fig. 6.12: Experimental setup for measuring transmission via surface waves.....  | 40 |
| Fig. 6.13: Measured transmission of TM surface waves on mushroom-like EBG and metal sheet.....   | 41 |
| Fig. 6.14: TM surface wave propagation on mushroom-like EBG: a) 9 GHz, b) 10 GHz, c) 15 GHz.....   | 41 |
| Fig. 6.15: TE surface wave propagation on mushroom-like EBG: a) 9 GHz, b) 10 GHz, c) 15 GHz.....   | 42 |
| Fig. 6.16: Modal analysis of GaAs substrate and Si substrate.....  | 43 |
| Fig. 6.17: The dimensions of the unit cell.....  | 43 |
| Fig. 6.18: Frequency response of reflection phase and surface wave transmission of the EBG structure.....  | 44 |
| Fig. 6.19: Dispersion diagram of the mushroom-like EBG structure.....  | 44 |
| Fig. 6.20: Radiation pattern of a simple patch antenna, a) XZ plane, b) YZ plane.....  | 45 |
| Fig. 6.21: Mutual coupling between two antenna radiators.....  | 46 |
| Fig. 6.22: Electric field distribution (z-component) on the antenna surface (left) and the antenna surface with mushroom-like EBG structure (right)..... | 47 |
| Fig. 6.23: The spacing $S$ between the antenna element and the surrounding mushroom-like EBG.....  | 47 |
| Fig. 6.24: The principle of the Fabry-Perot resonator.....   | 48 |
| Fig. 6.25: Dimensions of the PRS unit cell.....  | 49 |
| Fig. 6.26: Schematic of the superstrate antenna.....   | 49 |
| Fig. 6.27: Frequency response of the complex reflection coefficient of the superstrate.....  | 50 |
| Fig. 6.28: Frequency dependence of the transmission magnitude of the superstrate.....  | 50 |
| Fig. 6.29: Radiation patterns of the designed antenna with superstrate: a) XZ plane, b) YZ plane.....  | 51 |
| Fig. 6.30: Calculated gain improvement of the designed antenna.....  | 52 |
| Fig. 6.31: Resonant cavity formed by PEC and PRS (top), and AMC and PRS (bottom).....  | 53 |
| Fig. 6.32: Dimensions of the PRS unit cell.....  | 54 |
| Fig. 6.33: Schematic of the superstrate antenna.....   | 54 |
| Fig. 6.34: Frequency response of the complex reflection coefficient of the LC superstrate.....   | 54 |
| Fig. 6.35: Frequency response of complex reflection coefficient of the mushroom-like EBG.....  | 55 |
| Fig. 6.36: Dispersion diagram of the mushroom-like EBG structure.....  | 55 |

|   |    |
|---|----|
| Fig. 6.38: Calculated improvement of the gain of the designed antenna.....  | 57 |
| Fig. 7.1: The final THz antenna.....  | 59 |
| Fig. 7.2: Radiation pattern of the final antenna, a) XZ plane, b) YZ plane.....   | 60 |
| Fig. 7.3: Axial ratio in broadside direction of the final antenna.....  | 61 |
| Fig. 7.4: Calculated gain improvement of the final antenna.....   | 61 |
| Fig. 7.5: Geometry of the final structure.....  | 64 |
| Fig. 7.6: Frequency response of reflection phase and surface wave transmission of the mushroom-like EBG structure.....        | 64 |
| Fig. 7.7: Dispersion diagram of the mushroom-like EBG structure.....  | 65 |
| Fig. 7.8: Frequency response of reflection phase of the LC superstrate (black $h = \lambda/22$ , red $h = \lambda/300$ )..... | 65 |
| Fig. 7.9: Simulated and measured reflection coefficient of the final antenna.....   | 66 |
| Fig. 7.10: Measured axial ratio of the final antenna.....   | 66 |
| Fig. 7.11: Radiation patterns of fabricated antenna at 10 GHz a) XZ plane, b) YZ plane.....                                   | 67 |

## LIST OF TABLES

|   |    |
|---|----|
| Table 4.1: The relationship between polarizations and losses.....                                   | 17 |
| Table 5.1: Comparison of typical antenna radiators.....   | 22 |
| Table 5.2: Comparison of the interdigital electrode capacitance evaluated by different methods..... | 24 |
| Table 5.3: Simulation results for the dual-slot antenna.....  | 26 |
| Table 5.4: Simulation results for the four-leaf-clover-shaped dipole antenna.....                   | 28 |
| Table 5.5: Simulation results for the cross-slot patch antenna.....                                 | 31 |
| Table 6.1: Modal analysis of GaAs substrate and Si substrate.....                                   | 43 |
| Table 6.2: Simulation results for different configurations of EBG antennas.....                     | 46 |
| Table 6.3: Simulation results for simple antenna and antenna with superstrate.....                  | 52 |
| Table 6.4: Simulation results for antenna with LC superstrate.....                                  | 57 |
| Table 6.5: Comparison of different types of superstrates.....                                       | 57 |
| Table 7.1: Dimensions of the designed antenna.....  | 60 |
| Table 7.2: Simulation results for basic antenna and final one.....                                  | 61 |
| Table 7.3: Comparison of RF/microwave antennas and photoconductive ones.....                        | 62 |
| Table.7.4: Simulation and measurement results for final antenna.....                                | 67 |

## LIST OF ABBREVIATIONS

|         |  |
|---------|--|
| AMC     | Artificial Magnetic Conductor          |
| AR      | Axial Ratio                            |
| CCW     | Counter Clock Wise                     |
| CP      | Circularly polarized                   |
| CPW     | Coplanar Waveguide                     |
| CST     | Computer Simulation Technology         |
| CW      | Continuous wave                        |
| DC      | Direct Current                         |
| DNG     | Double-Negative                        |
| DPS     | Double-Positive                        |
| EBG     | Electromagnetic Band Gap               |
| ENG     | $\epsilon$ -Negative                   |
| FBR     | Front-to-Back Ratio                    |
| FSS     | Frequency Selective Surface            |
| GaAs    | Gallium Arsenide                       |
| GaSe    | Gallium Selenide                       |
| HIS     | High Impedance Surface                 |
| IDE     | Interdigital Electrode                 |
| InAs    | Indium Arsenide                        |
| InGaAs  | Indium Gallium Arsenide                |
| InP     | Indium Phosphide                       |
| LHCP    | Left Hand Circular Polarization        |
| LT-GaAs | Low-Temperature-Grown Gallium Arsenide |
| MNG     | $\mu$ -Negative                        |
| MSM     | Metal-Semiconductor-Metal              |
| MWS     | Microwave Studio                       |
| PC      | Photoconductive                        |
| PEC     | Perfect Electric Conductor             |
| PMC     | Perfect Magnetic Conductor             |
| PRS     | Partially Reflective Surface           |
| RF      | Radio Frequency                        |
| RHCP    | Right Hand Circular Polarization       |

|      |                     |
|------|---------------------|
| Si   | Silicon             |
| SOS  | Silicon-on-Sapphire |
| TE   | Transverse Electric |
| TM   | Transverse Magnetic |
| ZnTe | Zinc Telluride      |

# 1 INTRODUCTION

With wavelengths between  $\lambda = 1000 \div 300 \mu\text{m}$  (300 GHz to 10 THz), the terahertz range bridges the gap between the microwave region and the infra-red frequencies, being until recently one of the least explored regions of the electromagnetic spectrum (see Fig. 1.1). In this text the THz range is defined as a frequency range from 300 GHz to 3 THz (as defined in [1]). While both sides of the spectrum, optics and electronics, have a long history of research and development, leading to a huge amount of commercially available sources, detectors and many additional devices, the THz range is still in its beginnings. The reason for this might be an absence of practical sources of THz radiation. The delayed development is mainly due to the difficulty of producing reliable THz-wave generators delivering sufficient output power as well as sensors that can detect this radiation.

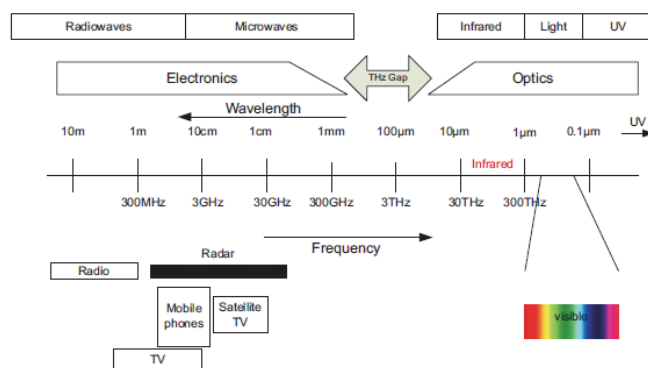


**Fig. 1.1:** Electromagnetic spectrum from radio frequency (RF) to ultra-violet (UV) [2].

For about 20 years (1970-1990), high-resolution spectroscopy and remote sensing of the Earth were the only driving forces for THz science [3]. Based on heterodyne and Fourier transform techniques, these methods offered astronomers, chemists and space scientists a tool for investigating the thermal emission lines of a wide diversity of light-weight molecules, as approximately one-half of the total luminosity and 98% of the photons emitted since the Big Bang have fallen into the submillimeter and far-infrared (P. Siegel, Jet Propulsion Laboratory) [4], [5], [6]. The THz frequency range is therefore frequently described as the "most scientifically useful yet least explored" [2].

Besides the rather traditional scientific application areas a large amount of other applications can also utilize the unique properties of the THz-wave region. Many new applications could be identified and some of them have a high commercial potential in the future. During the last decade, the general interest in THz radiation rose, mainly due to its ability to penetrate many organic materials, without the damage associated with ionizing radiation like X-rays. Since THz radiation is strongly absorbed by water molecules, it can be used to discernment between materials with varying water content. All these properties laid the basics for extensive applications in process and quality control [7] like biomedical imaging (T-ray imaging) [8]. Tests are currently under way to determine whether terahertz tomographic imaging can augment or replace mammography [9], and some scientists have proposed terahertz imaging as a method of screening passengers for explosives, weapons at airports [10]. By analyzing the

frequency dependence of the transmission or reflection intensity, each substance has a unique behavior, so called "Fingerprinting" that is assigning a spectral characteristic to each molecule or chemical [11]. One of the amazing properties of THz radiation is its ability to pass through a wide range of materials, making it possible to "see" through many materials such as paper, cardboard, textiles, plastics, wood and etc. This property allows nondestructive and noninvasive inspection of mail packages and envelopes in post offices, luggage and personal belongings in airports, border crossing points and etc. This is the reason why the THz-waves can be used in security applications.

## 2 STATE-OF-THE-ART

In, this chapter we present the state-of-the-art in the field of integrated THz emitter and receiver concepts.

The research is dominantly aimed to develop broadband and high efficiency continuous wave (CW) THz sources that can be used in compact semiconductor-based transmitter and receiver blocks. The general requirements cover low costs, tunability, small size, robustness and high spectral purity. High spectral purity can be ensured by CW sources which can produce output signals with a narrow line width over a broad frequency range [2].

The THz source generating submillimeter wave radiation is the key element of the integrated emitter/receiver. We therefore review different concepts of THz sources. The review comprises CW semiconductor photomixers and semiconductor diodes for CW THz generation [2], [12]. The review covers:

- Terahertz wave generation [2], [13];
- Photomixing [2], [14];
- Photoconductive mixers [2], [15], [16];
- p-i-n diodes [2], [17];
- Optical waveguide coupled photodiodes [2], [18];
- Optical rectification [2], [19];
- Surface emitters [20], [21];
- Uni-traveling carrier photodiode [22], [23].

### 2.1 Antennas for Integrated Photomixers

In general, integrated photomixers consist of a planar antenna and a hemispherical lens. The antenna is printed on the same substrate layer as the photomixer device. The lens is placed on the backside of the substrate layer. The lens is typically made of silicon [15].

Two antenna concepts can be applied when integrating with photomixers:

- Narrowband, resonant antenna structures;
- Broadband, frequency independent antennas.

In the thesis, a narrowband, resonant concept is applied.

When deciding about a specific antenna structure, the antenna impedance (input impedance), the radiation pattern, the polarization and the radiation efficiency are most important parameters to be considered.

Input impedance of resonant antennas is closely related to the frequency. Narrowband antennas exhibit a higher gain compared to broadband antennas. This is the main motivation for designing a resonant antenna. Since the output power of available THz sources is very low [2], [15], exploitation of a resonant antenna is the first issue, and correct impedance matching between the device and the antenna is the second issue.

In some cases, the device capacitance can be used to compensate the inductive behavior of the antenna under consideration. If the antenna operates slightly out of the resonance, its input susceptance can compensate the capacitive reactance of the photomixer. This approach, however, restricts the geometry of the device and the antenna. In general, matching is achieved by a standard line transformation with varying impedance [2].

The input resistance of the antenna might be satisfactorily high even if the antenna operates out of resonance [24], [25], [26]. In order to compensate the reactance of the device, we design an antenna out of the resonance.

Typical structures of narrowband resonant antennas to be potentially applied are:

- The dipole geometry [27];
- The dual-dipole geometry [27];
- The slot geometry [27];
- The dual slot geometry [22].

The conventional narrowband antennas for photoconductive mixers have the following fundamental properties:

- Linear polarization is produced;
- Dimensions correspond with the wavelength;
- Silicon lens is used for focusing radiated power;
- The radiating element exhibits lower gain;
- Side lobes are of a high level;
- Dimensions of the device are large due to a silicon lens.

For future security applications, the conventional narrow band antennas are not suitable since any antenna element has to be completed by a silicon lens to focus a beam. Fabrication of a silicon lens is expensive. Lens dimensions are immense compared to a radiating element. Moreover, the silicon lens does not support circular polarization for antenna matrix, which brings disadvantages in security applications.

This work is aimed to create a multilayer planar structure supporting circular polarization. Therefore, the silicon lens is required to be replaced by a purely planar structure called partially reflecting surface (PRS or superstrate). The basic principle of PRS is described in Chapter 4. PRS has not been published in the field of THz technologies yet. PRS can be used for narrow-band structures only due to narrowband characteristics of the superstrate (PRS) and a narrowband axial ratio (about 3 %).

### 3 OBJECTIVES

Here, we formulate the main objectives of the dissertation thesis and summarize all challenges resulting from the investigated problems.

Objective 1:

- *To propose a design procedure for circularly polarized antennas operating at (sub)millimeter-wave frequencies*

The main objective can be divided into three sub-goals:

- *To replace a silicone lens by a partially reflecting surface (PRS);*
- *To exploit photoconductive mixers for the excitation of an antenna operating at THz frequencies with circular polarization;*
- *To verify a requested high directivity and a wide axial ratio of the device experimentally.*

The work is aimed to propose a design procedure for a planar multilayer THz source exhibiting a circular polarization. Properties of such a source are going to be improved using a planar superstrate (PRS) (improving gain) and a mushroom-like EBG structure (suppressing surface waves, reducing sidelobe level). The design procedure can be used for narrow-band structures only due to narrowband characteristics of the superstrate and narrowband axial ratio.

Such a concept has not been published in the field of THz technologies yet.

## 4 NOVEL MULTI-LAYER THZ SOURCE

In this chapter, we will introduce a multi-layer concept of a circularly polarized (CP) THz source.

### 4.1 Circular polarization

A THz system with linear antennas both in a receiver and in a transmitter should keep the polarization plane unchanged for the best transmission. The fixed polarization plane can be kept in static applications (detection). But in security applications, the position of a hidden object can continuously move, rotate, etc. In a linearly polarized system, a polarization misalignment of  $45^\circ$  degrades the signal for up to 3 dB, and the misaligned of  $90^\circ$  attenuates the signal up to 20 dB.

The circularly polarized THz is immune against changes of the polarization plane. So, the quality of the detection stays perfect in all the cases. Table 4.1 shows the relationship between the horizontal polarization, the vertical polarization, the right hand circular polarization (RHCP) and the left hand circular polarization (LHCP) and losses in dB.

**Table 4.1:** The relationship between polarizations and losses.

|            | Horizontal | Vertical | RHCP   | LHCP   |
|------------|------------|----------|--------|--------|
| Horizontal | 0 dB       | -30 dB   | -3 dB  | -3 dB  |
| Vertical   | -30 dB     | 0 dB     | -3 dB  | -3 dB  |
| RHCP       | -3 dB      | -3 dB    | 0 dB   | -30 dB |
| LHCP       | -3 dB      | -3 dB    | -30 dB | 0 dB   |

### 4.2 Operating principle

Structure of the proposed THz source is shown in Fig. 4.1.

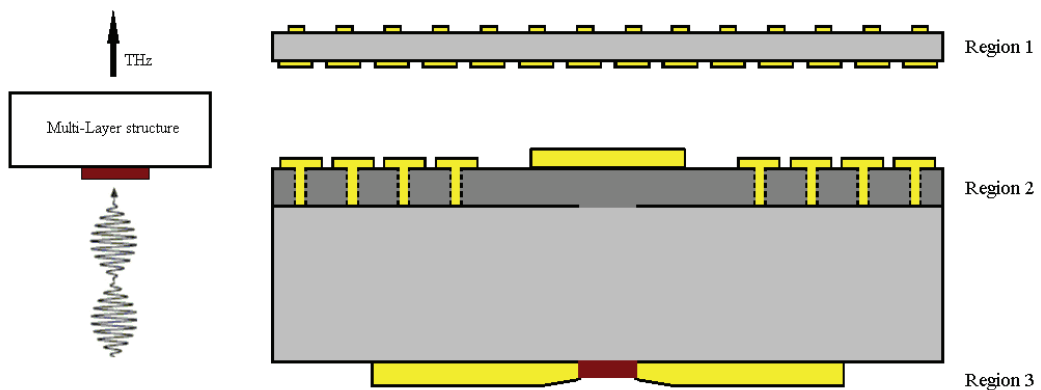


**Fig. 4.1:** Sketch of the proposed THz source.

The proposed THz antenna consists of three regions:

- Region 1: A partially reflective surface (a planar lens, a Fabry-Perot resonator);
- Region 2: A THz antenna with crossed slots and a mushroom-like EBG structure;
- Region 3: A photoconductive photomixer and a dual-slot antenna and a DC biasing.

In order to generate a circularly polarized wave, two laser sources are combined and focused on the photomixer. The resulting THz-modulated current is forwarded into an antenna [2], which emits CW THz radiation (emission) into surrounding space [2], [25], [26]. The THz emission passes through the (GaAs) substrate and irradiates the cross slots with different lengths which generate circular polarization. The multi-layer source requires a square patch on the top of the structure to achieve two orthogonal modes for CP operation ( $TM_{10}$  and  $TM_{01}$ ). Obviously, the resonant frequency of the square patch depends on the coupling.

In following chapters, a detailed description of partial layers is presented.

## 5 THZ SOURCE AND THZ CP ANTENNA

In this chapter, we discuss the photomixing theory and continue with the description of two types of the THz antennas: (1) the dual slot antenna and (2) the full wavelength dipole. These antennas play the role of the near-field source for the THz CP device.

### 5.1 Photomixing

An efficient generation of a continuous THz wave is difficult since neither optical technologies nor microwave ones can be applied here directly. Photomixers offer an interesting way to over-bridge the "THz gap" by combining both optical and electronic technologies. The basic principle of photomixing is depicted in Fig. 5.1.

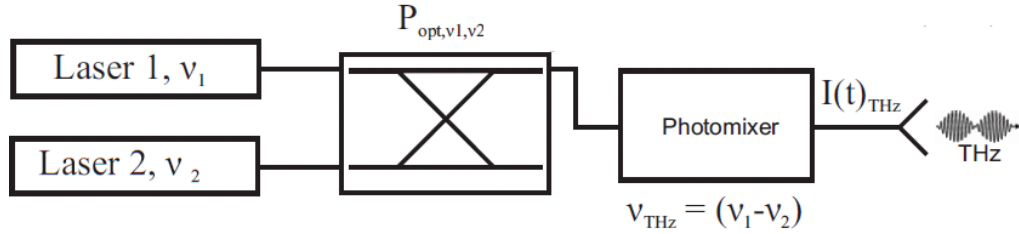


Fig. 5.1: Basic principle of photomixing.

Two laser sources are combined and focused on the photomixer. The THz frequency of the output wave corresponds to a differential frequency of laser sources. The fundamental mechanism is  $P_{\text{opt}} \sim I_{\text{photo}}^2$ , where no further harmonics are generated ideally [2].

Photomixing means the periodic generation of carriers in a photoconductor by a modulated laser beam. The superposition of two, in frequency slightly detuned laser-beams, leads to a beat signal with the difference frequency ( $\nu_{\text{THz}} = \nu_1 - \nu_2$ ) [2], [14], [24]. The modulated laser beam is absorbed in the semiconductor material and generates electrons and holes periodically, which are separated in an applied electric field. The resulting THz-modulated current is typically fed into an antenna [2], which emits CW THz radiation into the surrounding space [2], [25], [26]. The basic equation for the THz output power from photomixing assuming the antenna is perfectly matched to the device is defined as [2]:

$$P_{\text{THz}(\nu_{\text{THz}})} = \frac{1}{2} I_{\text{ph}}^2 R_A \frac{1}{1 + \left(\frac{\nu_{\text{THz}}}{\nu_{\text{RC}}}\right)^2} \cdot \frac{1}{1 + \left(\frac{\nu_{\text{THz}}}{\nu_{\text{tr}}}\right)^2}, \quad (5.1)$$

where  $I_{\text{ph}}$  is the generated AC-photocurrent,  $R_A$  is the antenna-resistance,  $\nu_{\text{RC}}$  denotes the RC-frequency of the photomixer and  $\nu_{\text{tr}}$  is the transit time frequency of the carriers, depending on their drift velocity and the distance they have to travel to get to the contacts. If one of the lasers is tunable, an ultra-wide tunability in frequency can be

obtained. An upper limitation on the tuning range is set by the  $v_{RC}$  and  $v_{tr}$  in (5.1). The generated time varying current is [2]

$$I(t) = I_0 [1 + \cos 2\pi\nu_{THZ}t], \quad (5.2)$$

$$I_0 = \frac{\eta_{ph} q P_L}{h\nu_0}, \quad (5.3)$$

where  $P_L$  is the output laser power and  $\eta_{ph}$  is fraction of the incident photons absorbed in the active region of the photomixer. The generated THz-photocurrent  $I(t)$  in (5.2) can provide the input signal to an antenna structure radiating the generated power.

## 5.2 Photoconductive mixers

Photoconductive mixers were the firstly developed semiconductor THz sources. These devices held for a long time the record with respect to the output power, which was in the area of few  $\mu\text{W}$  [15]. Photoconductive mixers are typically made of interdigital electrodes (MSM-structures) placed on a low-temperature-grown GaAs (LT-GaAs), which exhibits very short recombination lifetimes. In the gaps between the fingers (electrodes) (see Fig. 5.2), carriers are generated and afterwards separated by an applied electric field, which the structure is biased with [2].

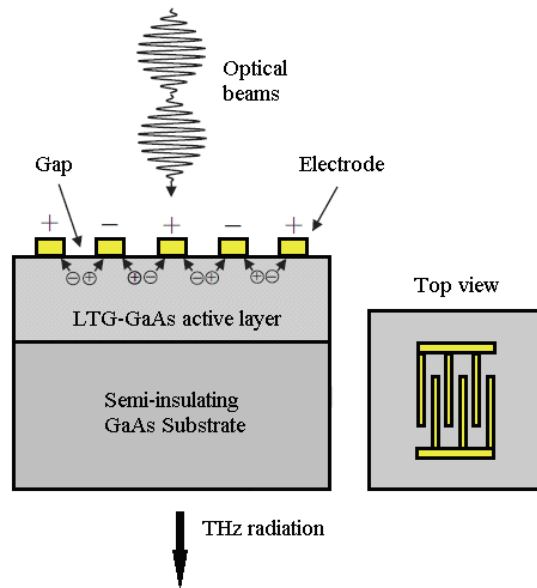


Fig. 5.2: LT-GaAs photomixer.

The recombination lifetimes have to be short so that the photo-carriers generated in the previous period are recombined until the next period starts (0.2 to 1.0 ps) [2]. The devices have small distances of about  $1 \mu\text{m}$  between the fingers [2], so the transit-time  $\tau_{tr}$  is about 10 ps, when assuming the carriers are moving at their saturation drift velocity of  $v_{sat} \approx 10^7 \text{cm/s}$ . The saturation drift velocity of  $v_{sat} \approx 10^7 \text{cm/s}$  is reached when high-intensity electric fields are applied to the photoconductor [15], [16].

Another limitation factor is the recombination time  $\tau_{rec}$  of the generated carriers since these carriers have to arrive to the contacts before recombining again. Hence

a trade-off between the transit time and the recombination time exists where the frequency dependence of the device can be improved by reducing the recombination time or the transit time. This results in the reduced output power since not all the generated carriers arrive to the contacts [2], [15]. The main problem of the photoconductor concept is the capacitive roll-off on one hand and a low photoconductive gain  $g = \tau_{\text{rec}} = \tau_{\text{tr}}$  on the other hand. The photoconductive gain is given by the recombination lifetime  $\tau_{\text{rec}}$  of the LT-GaAs and the transit-time  $\tau_{\text{tr}}$  of the carriers until they reach the contacts [2], [16].

To summarize, a LT-GaAs based photomixer has a best reported output power of  $2 \mu\text{W}$  at 1 THz. The upper limit performance expected for an optimized LT-GaAs photomixer at 1 THz is  $100 \mu\text{W}$  [2], but an intensive technological effort is still necessary to reach this goal.

### 5.3 THz source overview

The role of the CW THz source can be played by the THz photomixer which transforms the THz beat signal of the incident laser wave into THz waves using a photoconductor and an antenna. The Figure 5.3 shows the equivalent circuit of the THz photomixer antenna.

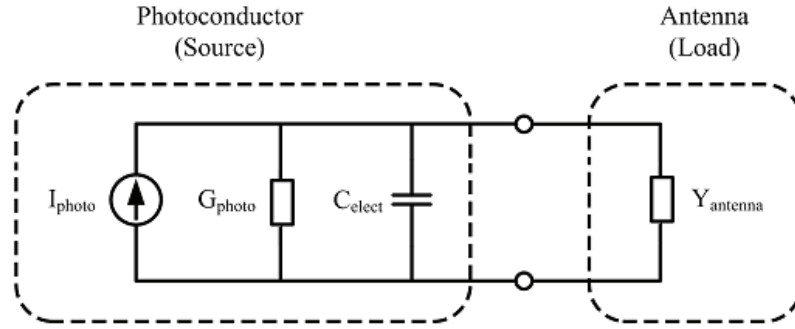


Fig. 5.3: Equivalent-circuit model of the photomixer antenna.

The photocurrent is produced by a set of photocurrent sources  $I_{\text{photo}}$ . In parallel to the current source, a photo-conductance  $G_{\text{photo}}$  of the mixer, a capacitance of electrodes  $C_{\text{elect}}$  and an input admittance of the antenna  $Y_{\text{antenna}}$  are connected. Under photomixing conditions, the photo-conductance  $G_{\text{photo}}$  is normally smaller than  $(10 \text{ k}\Omega)^{-1}$  because of the use of the CW laser as an excitation source. This phenomenon causes a serious mismatch between the photomixer and the antenna. Therefore, the antenna for a THz photomixer is requested to exhibit only high radiation efficiency but too a high input resistance. In the antenna design, the total efficiency  $\epsilon_{\text{total}}$  is the product of the radiation efficiency  $\epsilon_{\text{radiation}}$  and the matching efficiency  $\epsilon_{\text{match}}$ , and can be expressed as:

$$\epsilon_{\text{total}} = \epsilon_{\text{radiation}} \cdot \epsilon_{\text{match}} = \epsilon_{\text{radiation}} \cdot (1 - |\Gamma|^2), \text{ where} \quad (5.4)$$

$$\Gamma = \frac{Z_{\text{antenna}} - Z_{\text{photomixer}}}{Z_{\text{antenna}} + Z_{\text{photomixer}}}, \quad (5.5)$$

$Z_{\text{antenna}}$  is input impedance of the designed antenna and  $Z_{\text{photomixer}}$  is impedance of the

LT-GaAs photomixer. Hereafter, the matching efficiency is calculated by assuming photomixer impedance  $Z_{\text{photomixer}}$  and the corresponding total efficiency.

Employing a high impedance antenna for the THz source helps to maximize the radiated power. A narrow band antenna can be designed to match any impedance. Therefore, different types of antenna geometries have been investigated to maximize the antenna impedance. The input impedances were compared for antenna with equal characteristic width of the conductors and slots without considering the influence of dielectric. The results are summarized in Table 5.1.

**Table 5.1:** Comparison of typical antenna radiators.

| Antenna type                               | Typical impedance                |
|--|----------------------------------|
| Half-wave dipole                           | 73 $\Omega$                      |
| Full-wave dipole                           | 710 $\Omega$                     |
| Folded dipole                              | 250 $\Omega$                     |
| <b>Four-leaf-clover-shaped dipole [28]</b> | <b>1 890 <math>\Omega</math></b> |
| Half-wave slot                             | 530 $\Omega$                     |
| Full-wave slot                             | 50 $\Omega$                      |
| Folded slot                                | 130 $\Omega$                     |
| <b>Dual slot [27]</b>                      | <b>452 <math>\Omega</math></b>   |

For further investigation, the dual-slot antenna and the four-leaf-clover shaped dipole were selected. The details will be given in following subchapters.

The output power of conventional photomixers is limited by a large difference of impedances between the antenna and the photomixer (10 k $\Omega$  versus 100 k $\Omega$ ). This mismatch causes losses up to 98%.

The photomixer impedance at the operating frequency is [33]:

$$Z_{\text{photomixer}} = \frac{V_{\text{bias}}}{I_{\text{photo}} \left( \frac{1}{1 + (\Delta\omega + \tau_e)^2} \right)^{\frac{1}{2}}}, \quad (5.6)$$

where  $V_{\text{bias}}$  is the bias voltage across the photoconductor electrodes,  $I_{\text{photo}}$  is the DC photocurrent and  $\tau_e$  is the photo-carrier lifetime of the semiconductor.

#### 5.4 Dual-slot antenna like THz source

A low output power of a photomixer at higher frequencies is a result of -6 dB/octave roll-off arising from the lifetime of the carriers and a reduction in load impedance. The photomixer exhibits a capacitive behavior.

The generated terahertz radiation can excite dipoles if a large bandwidth is not

required [29]. The interdigital electrode (IDE) capacitance of the photomixer increases the antenna resistance. Moreover, we can change the IDE capacitance to tune the system for the operation at a given frequency. For slot antenna elements, an inductive tuning is beneficial. In order to tune the system, the IDE capacitance at the desired frequency has to be accurately calculated [29].

The equivalent circuit model of the IDE is based on a pure capacitive  $\pi$  network as shown in Fig. 5.4. Whereas the IDE capacitance  $C_{\text{elect}}$  depends on the size and the number of fingers of the electrode, the parasitic capacitances  $C_{p1}$  and  $C_{p2}$  do not depend on these parameters. Parasitic capacitances can be minimized by varying the location of ground planes [30].

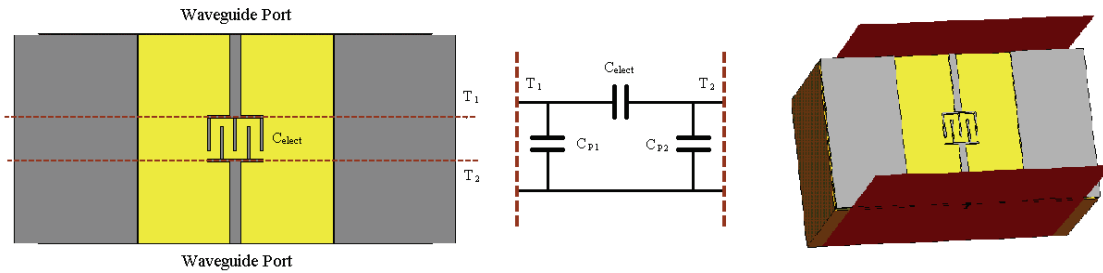


**Fig. 5.4:** CST model of an IDE photomixer and equivalent capacitor  $\pi$ -network.

An interdigital electrode capacitance  $C_{\text{elect}}$  is of prime interest for tuning purposes. The capacitance can be determined from Y-parameters:

$$C_{\text{elect}} = \frac{-\text{IMAG}\{Y_{12}\}}{2\pi f}. \quad (5.6)$$

Here,  $f$  is the operating frequency and  $Y_{12}$  is the reverse trans-conductance. The use of this approach makes the calculation of the interdigital electrode capacitance  $C_{\text{elect}}$  independent of any structural geometry between two reference planes  $T_1$  and  $T_2$ .

The numerical calculation of  $C_{\text{elect}}$  has been compared with two analytical transcripts. Both the transcripts are based conformal mapping. The first one was calculated by C. Sydlo [31], and the second one was published in [32]. A test model was created for verification (see Fig 5.5). Achieved results are given in Table 5.2.

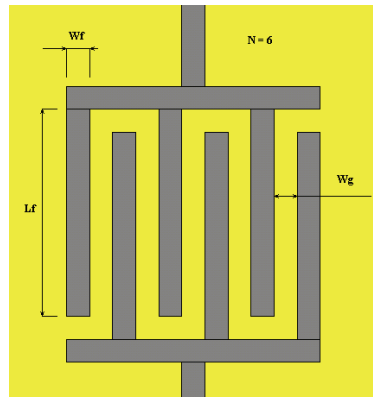


**Fig. 5.5:** Test capacitor:  $W_f = 1\mu\text{m}$ ,  $L_f = 9\mu\text{m}$ ,  $W_g = 1\mu\text{m}$ ,  $N = 6$ .

**Table 5.2:** Comparison of the interdigital electrode capacitance evaluated by different methods.

| Approach ( $f = 1$ THz)    | Value of the capacity [fF] |
|----------------------------|----------------------------|
| Conformal Mapping [30]     | 3.024                      |
| Simple Approximation [32]  | 7.912                      |
| CST MWS (frequency solver) | 3.046                      |
| Published results [31]     | 3.061                      |

The systematic design procedure of a dual-slot antenna is referred in [30].

The dual-slot antenna is fed by discrete port  $Z_{\text{port}} = 10 \text{ k}\Omega$  with a parallel lumped capacitor. The capacitance was computed from physical dimensions of the photomixer (see Fig. 5.5). The coordination system of the proposed antenna is shown in Fig. 5.6.

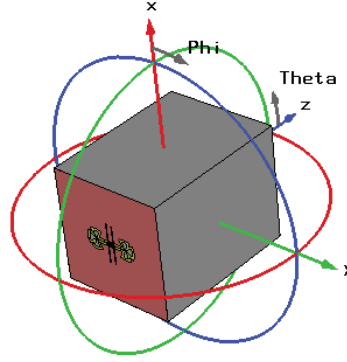


**Fig. 5.6:** The coordination system of the proposed antenna.

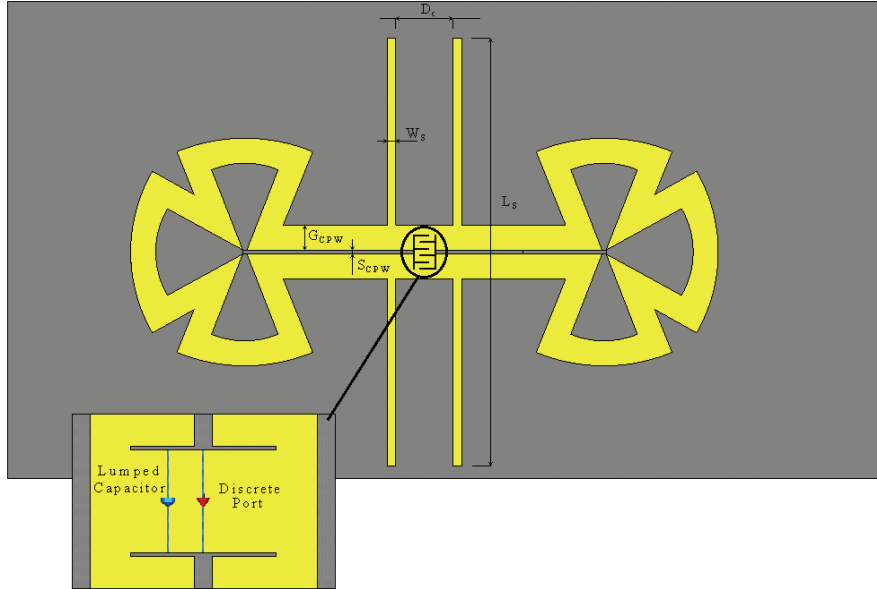


**Fig. 5.7:** Designed dual-slot antenna.

The designed antenna is shown in Fig. 5.7. The length of the couple of slots equals to  $L_S = 103 \text{ }\mu\text{m}$ , the width of slots is  $W_S = 2 \text{ }\mu\text{m}$  and thickness of metallization equals to  $t = 0.250 \text{ }\mu\text{m}$ . The designed antenna is placed on a GaAs substrate with the thickness

$h_{\text{GaAs}} = 400 \text{ } \mu\text{m}$  and the relative permittivity  $\epsilon_{r1} = 12.94$ . Dealing with the coplanar waveguide (CPW) feeding line, the width of the central strip is  $S_{\text{CPW}} = 1 \text{ } \mu\text{m}$ , the width of gaps is  $G_{\text{CPW}} = 6 \text{ } \mu\text{m}$  and the characteristic impedance equals to  $Z = 89 \text{ } \Omega$ . The distance between slots in the couple is  $D_C = 13.76 \text{ } \mu\text{m}$ .

The use of a correct biasing scheme plays a pivotal role in determining the overall efficiency of the THz emitter. The THz leakage down the bias line can be minimized using choke filters. The RF choke containing the 3-fan CPW radial stub approach is shown in Figure 5.8. The central stub of a 3-fan CPW radial stub scheme is a DC bias pad.

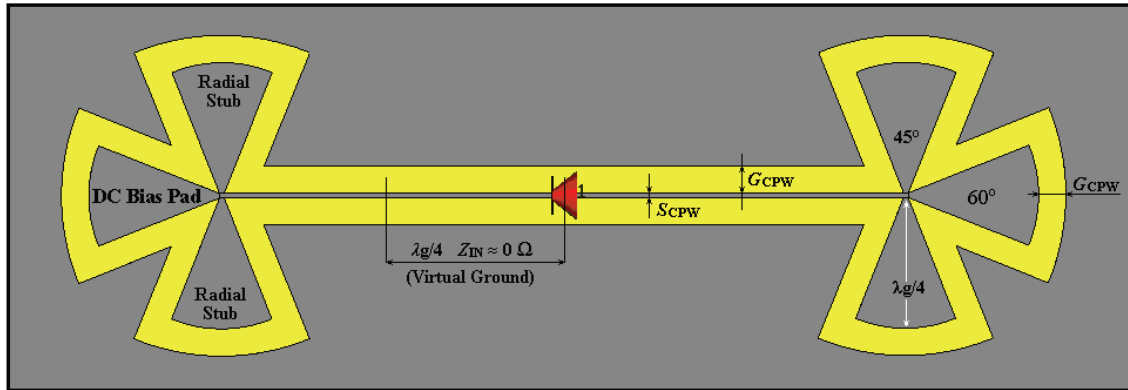


**Fig. 5.8:** RF choke filter without dipole arms.

THz signal can be prevented from escaping through the DC network by exploiting a  $\lambda_g/4$  or  $3\lambda_g/4$  transmission line, in conjunction with a  $\lambda_g/4$  radial stub (short end is transformed by a transmission line of length  $\lambda_g/4$  or  $3\lambda_g/4$  to an open circuit).

THz short circuit is created at the point, where the  $\lambda_g/4$  radial stub is connected to the transmission line. The THz signal experiences very low impedance at this point (virtual ground). The connection of this low impedance to a  $\lambda_g/4$  or  $3\lambda_g/4$  transmission line results in a high impedance (open circuit) point, at the opposite end of the transmission line [34].

The input impedance was increased by a lossy gold conductor. The virtual ground is determined to be  $10 \text{ } \Omega$  with a small imaginary part of impedance. Ideally, the input impedance should be  $0 \text{ } \Omega$ . However, the input impedance of 2 to 3  $\Omega$  can be achieved by varying angles and radii of three radial stubs [29].

Figure 5.9 shows radiation patterns of the designed structure and obtained results are summarized the Table 5.3.

The full model of the dual-slot THz emitter was replaced by a near-field source. The presented simulations exploit a near-field source instead of a full model of the dual-slot antenna. The simulation approach with the near-field source was described in [35]. The approach benefits in saving the simulation time and providing a reasonable accuracy. The comparison of the full wave model and the near-field method is show in Fig. 5.8 for the situation when an antenna element is irradiated by a dual-slot antenna and with the near-filed source.

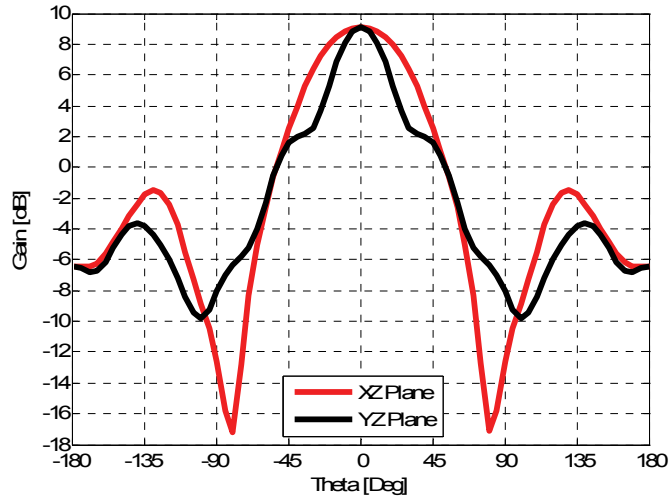


Fig. 5.9: Radiation patterns of the dual-slot antenna like THz source.

Table 5.3: Simulation results for the dual-slot antenna.

| Parameters $f=1$ THz (without lens) | Value    |
|-------------------------------------|----------|
| Main lobe magnitude                 | 9.1 dB   |
| Side lobe level in XZ plane         | -10.6 dB |
| Side lobe level in YZ plane         | -12.8 dB |
| Angular width (3 dB) in XZ plane    | 62.4°    |
| Angular width (3 dB) in YZ plane    | 34.8°    |
| Radiation efficiency                | 61.4 %   |

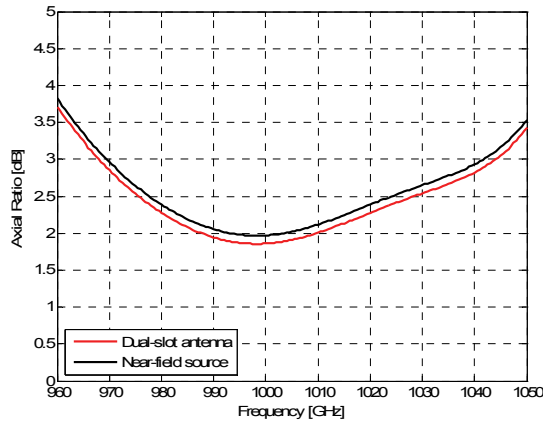


Fig. 5.8: Frequency response of axial ratio for different feeding techniques.

## 5.5 Four-leaf-clover-shaped dipole like THz source

Four-leaf-clover-shaped dipole is a special type of a full-wave dipole with bended radiating arms. The input resistance of this structure is 6-times higher compared to the conventional full-wavelength dipole. Hence, the mismatch between the photomixer and the antenna can be significantly improved [36]. Figure 5.9 shows the structure of the

designed THz photomixer consisting of an antenna as a radiating element and a bias circuit as a DC power supply element.

The considered four-leaf-clover-shaped antenna [36], [37] in the full-wavelength resonance is of following parameters: the width  $L_X = 35 \mu\text{m}$ , the length  $L_Y = 37 \mu\text{m}$ , gaps  $G_X = G_Y = 2 \mu\text{m}$ , and the width of the line  $W = 3 \mu\text{m}$ . Conductivity of the metal layer is  $1.6 \cdot 10^7 \text{ S/m}$  and its thickness is  $0.250 \mu\text{m}$ . The antenna is placed on a GaAs substrate ( $\epsilon_{r1} = 12.94$ ,  $h_{\text{GaAs}} = 500 \mu\text{m}$ ).

A quarter-wave choke is a conceived as a stepped-impedance filter consisting of high- and low-impedance sections. The length of each high- and low-impedance section corresponds to  $\lambda_g/4$ . The choke filter is employed to present a ‘‘short circuit’’ for the THz current at the interface with the radiating element. The length of each section can be slightly tuned away from  $\lambda_g/4$  to achieve the optimal operation at the operating frequency [38]. The line length  $L_{\text{High}} = 30 \mu\text{m}$  and the space  $G_{\text{High}} = 31 \mu\text{m}$  correspond to the high-impedance line. The line length  $L_{\text{Low}} = 30 \mu\text{m}$  and the space  $G_{\text{Low}} = 2 \mu\text{m}$  correspond to the low-impedance line. The total length of the bias line  $L_{\text{Bias}} = 600 \mu\text{m}$  and  $N = 4$  repetitions are considered.

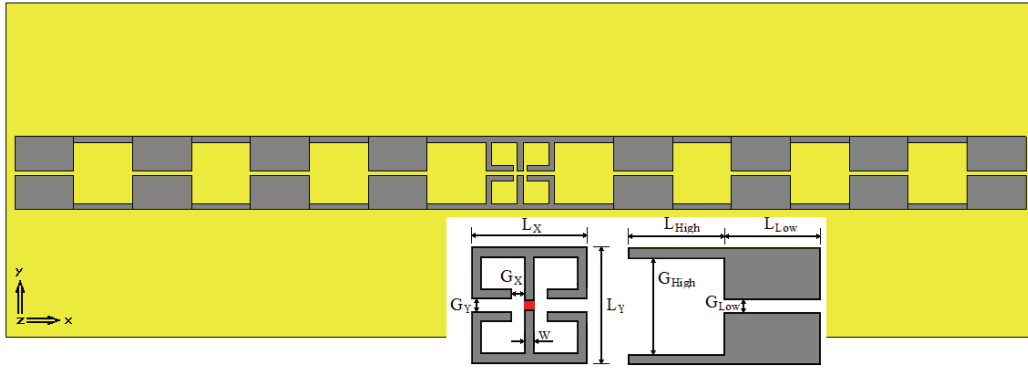


**Fig. 5.9:** The designed four-leaf-clover-shaped dipole antenna and biasing scheme.

Figure 5.10 shows the input impedance of the designed antenna. Figure 5.11 shows radiation patterns of the designed structure. Obtained results are summarized in Table 5.4.

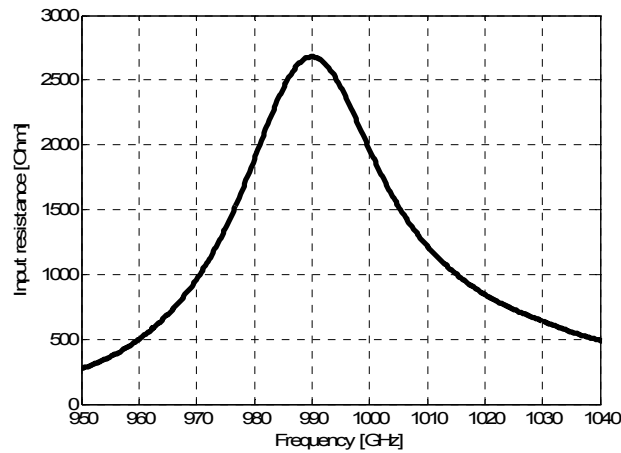


**Fig. 5.10:** Input resistance of the designed antenna.

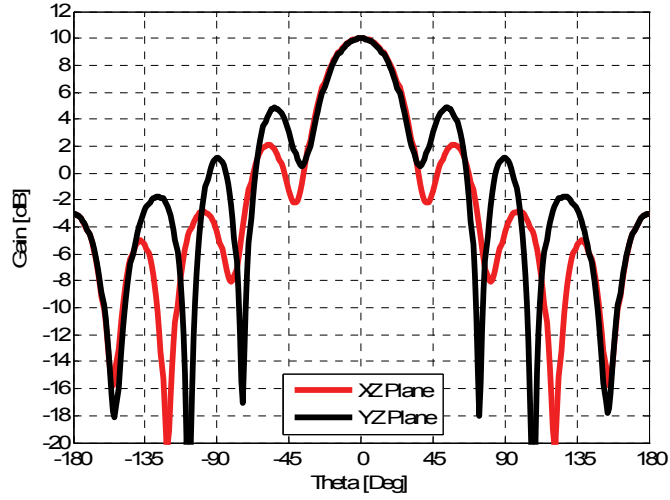


**Fig 5.11:** Radiation patterns of the four-leaf-clover-shaped dipole antenna like THz source.

**Table 5.4:** Simulation results for the four-leaf-clover-shaped dipole antenna.

| Parameters $f = 1$ THz (without lens) | Value   |
|---------------------------------------|---------|
| Main lobe magnitude                   | 10.0 dB |
| Side lobe level in XZ plane           | -7.6 dB |
| Side lobe level in YZ plane           | -5.1 dB |
| Angular width (3 dB) in XZ plane      | 44.2°   |
| Angular width (3 dB) in YZ plane      | 42.3°   |
| Radiation efficiency                  | 91.9 %  |

## 5.6 The CP THz cross-slot patch antenna

The thesis is aimed to design a circularly polarized THz antenna. Hence, the question "How circular polarization can be created using a linearly polarized THz source" is going to be answered.

The fundamental idea is illustrated by Fig. 5.12. The linearly polarized THz source produces THz emission. The emission passes through the GaAs substrate, and irradiates crossed slots of different lengths. The crossed slots excite two near-degenerate orthogonal modes for CP operation ( $TM_{10}$  and  $TM_{01}$ ) on the radiating patch element. The square patch radiates the CP THz wave into the surrounding space.

Resonant frequency of the square patch decreases with the increasing length of coupling slots [37]. The procedure used to design the circularly polarized THz antenna is based on the concept of partial independence of the resonances. The fundamental resonant frequency of the square patch can be split into two degenerated resonant modes  $TM_{10}$  and  $TM_{01}$  with a nearly equal amplitudes and 90° phase difference. Then, the resonant frequency of the resonant mode in the direction of the shorter slot is slightly lower than the frequency of the mode in the direction of the longer slot. If  $L_{S2} > L_{S1}$ , the left-hand circular polarization can be obtained, and vice versa.

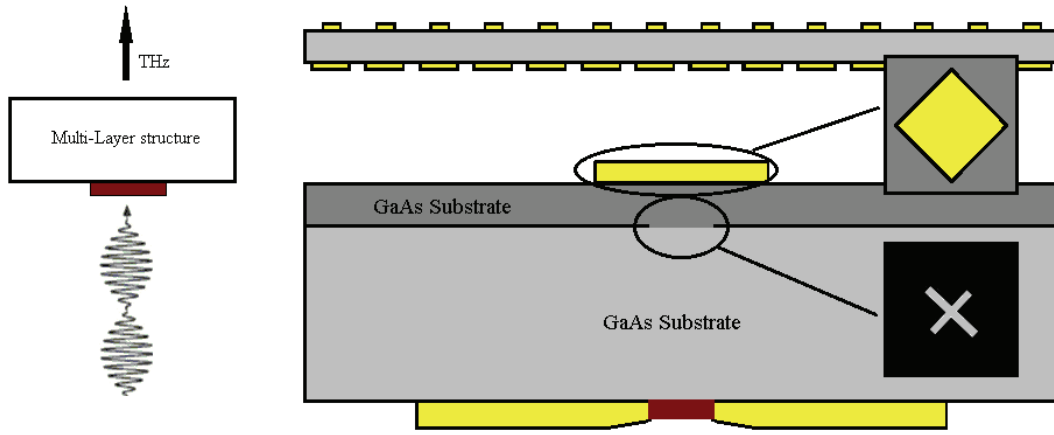


**Fig. 5.12:** Principle of creating circularly polarized wave.

The crossed slots for a specified center frequency  $f_{CP}$  are designed in two steps:

- The longer slot is assigned to resonate at  $f_1 = f_{CP} - f^1$ ;
- The shorter slot is assigned to resonate at  $f_2 = f_{CP} + f^2$ .

where  $f^1 \approx f^2 \ll f_{CP}$ . The frequencies  $f_1$  and  $f_2$  correspond to resonant modes  $TM_{10}$  and  $TM_{01}$ . The slots are designed and optimized separately. Each slot forms an angle  $45^\circ$ . Infinite lateral dimensions are assumed to avoid resonances resulting from the finite dimensions of the structure. The structure can be analyzed by Ansoft Designer to obtain optimum lengths of slots for the desired resonant frequencies separately.

Finally, the slots are put together and placed under the square patch. The overall performance of the structure is almost identical to the superposition of the performance of two slots thanks to the polarization diversity. Thereafter, the full structure is placed on the near-field representation of the THz source.

The proposed antenna is shown in Fig. 5.13. The square patch with the side length  $L_P = 29.02 \mu\text{m}$  is etched on a GaAs substrate ( $\epsilon_2 = 12.94$ ,  $h_2 = 15 \mu\text{m}$ ). The patch is excited via the cross-slot aperture. Lengths of arms of the cross are  $L_{S1} = 24.68 \mu\text{m}$  and  $L_{S2} = 36.05 \mu\text{m}$ . The centre of the cross and the centre of the patch have identical coordinates.

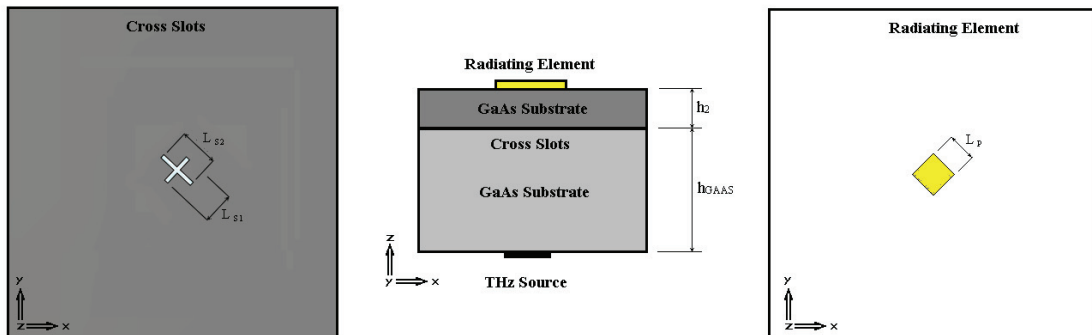
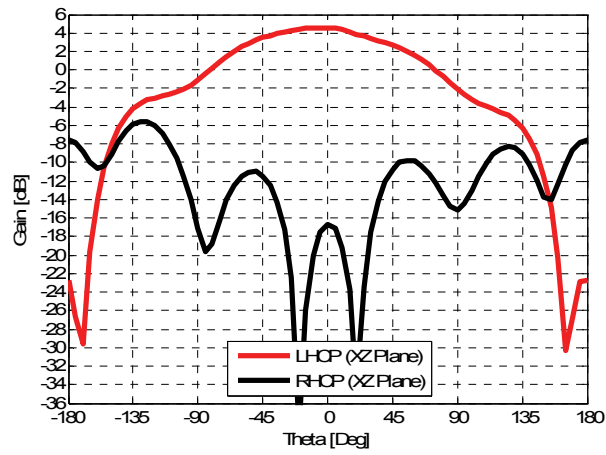
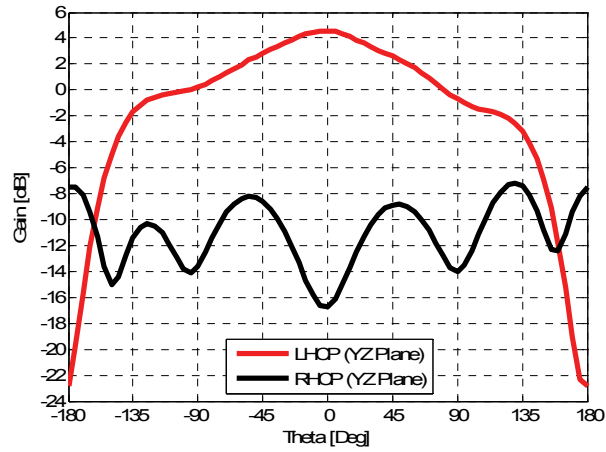


**Fig. 5.13:** Geometry of the designed antenna.

Figure 5.14 shows radiation patterns of the cross-slot patch antenna in E plane and H plane. Figure 5.15 shows axial ratio of the designed antenna. Obtained results are summarized in Table 5.5.



a)



b)

**Fig. 5.14:** Radiation pattern of the CP THz cross-slot patch antenna, a) XZ plane, b) YZ plane.

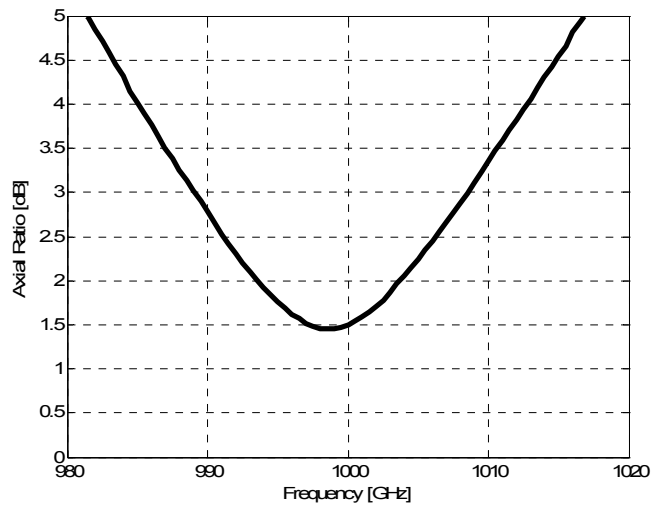


**Fig. 5.15:** Axial ratio in broadside direction of the CP THz cross-slot patch antenna.

**Table 5.5:** Simulation results for the cross-slot patch antenna.

| Parameters $f=1$ THz (without lens)           | Value   |
|---|---------|
| Main lobe magnitude                           | 4.6 dB  |
| Side lobe level in XZ plane                   | -5.9 dB |
| Side lobe level in YZ plane                   | -5.5 dB |
| Angular width (3 dB) in XZ plane              | 132.4°  |
| Angular width (3 dB) in YZ plane              | 136.1°  |
| Radiation efficiency (with near-field source) | 77.7 %  |

The CP THz antenna and an inter-digital electrode (IDE) can be represented by an equivalent circuit (Fig. 5.16). In the model of the antenna, we assume  $TM_{10}$  and  $TM_{01}$  excitation modes simultaneously to achieve circular polarization. Considering the  $TM_{10}$  mode, the current on the patch is assumed to flow horizontally over the length of the patch. Considering the  $TM_{01}$  mode, the current can flow over the width of the patch.

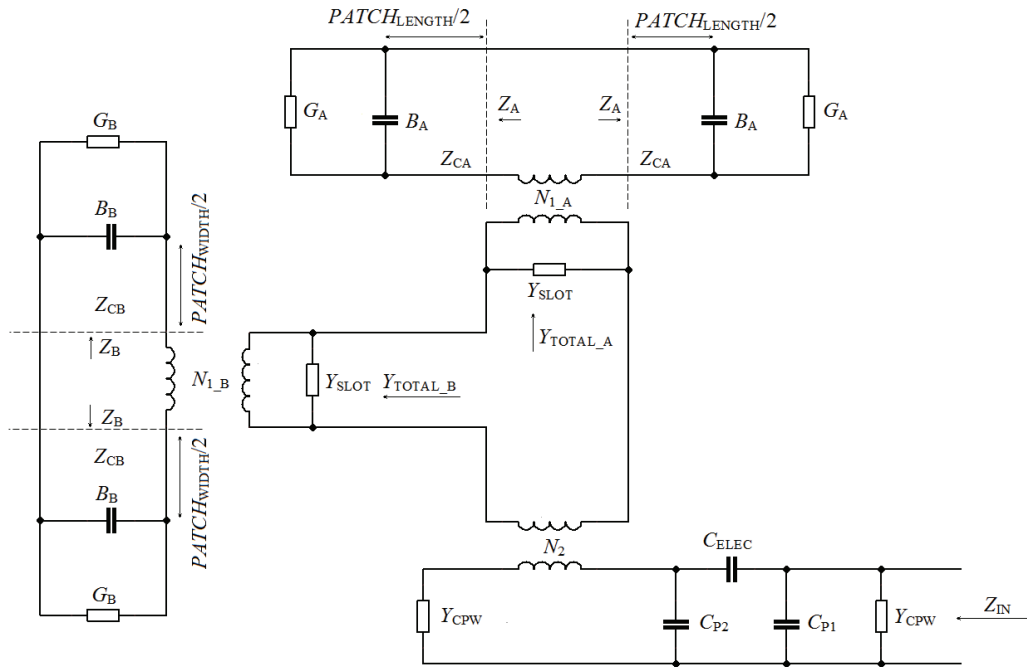


**Fig. 5.16:** Equivalent circuit model of the designed antenna.

Correspondingly, we assume two antenna elements as referred in Fig. 5.16. The first one has slot impedance  $Z_{CA}$ , characteristic impedance  $Z_A$  and propagation constant  $\gamma_A$ . The second one has slot impedance  $Z_{CB}$ , characteristic impedance  $Z_B$  and propagation constant  $\gamma_B$ . All unknown values can be calculated using equations given in [39], [40].

## 5.7 Summary

In this section, two types of THz source were described, the dual-slot antenna and the four-leaf-clover-shaped dipole. The biasing scheme for each antenna was described.

We presented here also a technique of calculating the parasitic capacitance of the photoconductive mixer depending on the substrate and the geometry of electrodes [29].

The four-leaf-clover-shaped dipole was able to provide very high input impedance. This antenna is therefore suitable for the connection to the LT-GaAs photomixer.

On other hand, the four-leaf-clover-shaped dipole is of a complicated geometry and radiation patterns show very high level of side lobes. Results reached by this type of antenna were published in [37].

In the following parts of the thesis, the dual-slot antenna is used [29].

The operating principle of the CP THz antenna was described and advantages of this antenna were discussed and published in [37].

## 6 PERIODIC STRUCTURES AND PLANAR LENS

This chapter is focused on the suppression of surface waves. We describe the principle and design a metallo-dielectric electromagnetic band gap (EBG) structure. In the following subchapter, we present the procedure of designing a planar lens and a cavity reduction.

### 6.1 Overview of metallo-dielectric periodic structures

Metallo-dielectric periodic structures have been described in many papers; e.g. [41], [42], [43], [44], [45], [46], [47]. Nowadays, metallo-dielectric periodic structures are frequently used as electromagnetic band gap (EBG) structures because of easy fabrication and compatibility with microwave circuits.

The general circuit representation of a metallo-dielectric unit cell is shown in Fig. 6.1. If the period (the lattice constant)  $D \ll \lambda$  then the effective permittivity and the effective permeability of the periodic media can be expressed using the series impedance  $Z$  and the shunt admittance  $Y$  of the unit cell [44], [47]:

$$\epsilon_{eff} \cdot \epsilon_0 = \frac{Y}{j\omega D}, \quad (6.1)$$

$$\mu_{eff} \cdot \mu_0 = \frac{Z}{j\omega D}, \quad (6.2)$$

Four types of periodic structures can be defined depending on the character (L, C) of series components and shunt components of the unit cell:

- DPS (double-positive);
- ENG ( $\epsilon$ -negative);
- MNG ( $\mu$ -negative);
- DNG (double-negative).

Possible implementations and related equivalent circuits of metallo-dielectric periodic structures are shown in Fig. 6.1 [44].

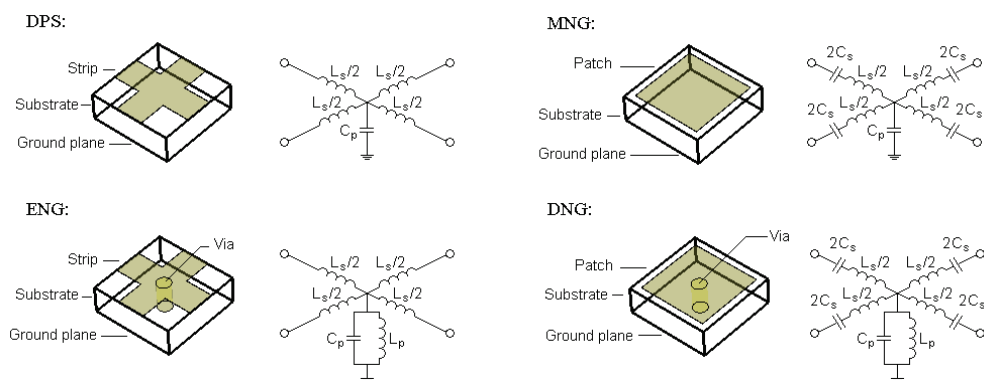


**Fig. 6.1:** Metallo-dielectric periodic structures.

The DPS structure can be implemented in the form of a 2D mesh of microstrip lines representing a series inductance and a shunt capacitance. For creating the ENG structure, we have to add a shunt inductance using a shorting via.

In order to implement the MNG structure, we can use a metallic patch (a series inductance, a series capacitance to neighboring cells, and a shunt capacitance to the ground plane). The DNG structure can be composed from a metallic patch with a shorting via (the pin adds the shunt inductance) [44].

The MNG and DNG structures are frequently exploited. Whereas the MNG is able to suppress transversally electric waves (TE), the DNG is able to suppress transversally magnetic waves (TM) [44].

## 6.2 Surface waves

Surface waves are excited at the interface between the dielectric substrate  $\epsilon_r > 1$  and air. Propagation of surface waves can be explained by partial reflections (see Fig 6.2). Reflections are limited by elevation angles lying in between  $\pi/2$  and  $\sin^{-1}(1/\sqrt{\epsilon_r})$ .

Surface waves can contribute to the coupling among antennas on the same substrate. Since surface waves decay with  $1/\sqrt{\epsilon_r}$ , the decrease of coupling follows this relation also.

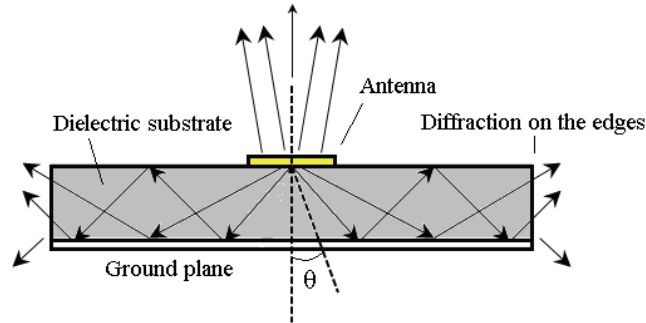


**Fig. 6.2:** Propagation of surface waves inside the grounded dielectric substrate.

Surface waves can be transversally magnetic (TM) or transversally electric (TE). TM and TE surface waves have a real propagation constant above the cutoff frequency.  $TM_0$  is the lowest TM wave with zero cutoff frequency.  $TM_0$  is excited at the open end of the microstrip antenna.  $TM_0$  propagates on very thin substrate of low permittivity. The velocity of propagation of  $TM_0$  is close to the velocity of light.

Cutoff frequencies of higher-order modes  $TM_n$  and  $TE_n$  are given by

$$f_c = \frac{nc}{4h \cdot \sqrt{\epsilon_r - 1}}, \quad (6.1)$$

where  $c$  is the velocity of light in free space,  $h$  is the thickness of the substrate and  $n = 1, 3, 5$  for  $TE_n$  waves and  $n = 0, 2, 4$  for  $TM_n$  waves.

$TE_1$  can propagate below the patch metallization, and can always be excited above the cutoff frequency.

Surface waves can be successfully suppressed by periodic structures exhibiting negative permittivity (TM wave suppression) or the negative permeability (TE wave suppression) in a specific frequency band.

For TM waves, the surface impedance exhibits inductive behavior. If the thickness of the dielectric substrate corresponds to one-quarter of the wavelength approximately (equation 6.1), the surface impedance exhibits capacitive behavior and the first  $TE_1$  wave occurs. However, the TM wave is still propagating. The TM wave simply adjusts its position toward the ground plane and the apparent surface impedance remains inductive [42], [48].

### 6.3 Analysis and design of mushroom-like EBG structures

The mushroom-like EBG structure is able to suppress propagation of surface waves by creating the forbidden zone (the band gap) at the resonant frequency. The band gap can suppress TM waves.

A mushroom-like EBG structure consists of three elements: a metal patch, a ground plane, and via (see Fig. 6.3). The mushroom-like EBG is described by the lattice constant  $D$ , the width of the gap  $g$ , thickness of the substrate  $h$ , radius of via  $R_{\text{via}}$  and relative permittivity of the substrate.

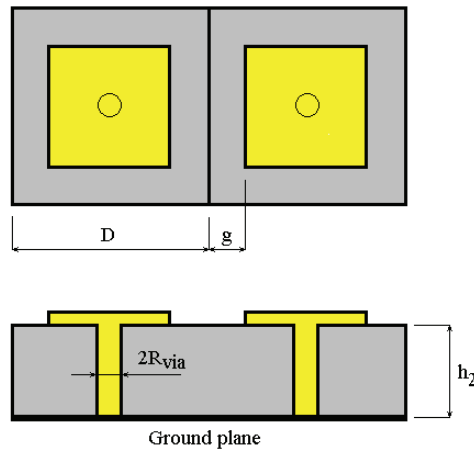


**Fig. 6.3:** Configuration of the mushroom-like EBG structure.

In this case, the presence of vertical pin is immediately necessary for the correct function of the mushroom structure. The dominant  $TM_0$  wave has no cutoff and propagates from zero frequency, with increasing frequency, the TM wave progresses deeper into dielectric substrate the surface impedance becomes to capacitive behavior and the first  $TE_1$  wave occurs. The vias create the necessary periodic structure inside the dielectric substrate and TM waves are suppressed effectively. At the same time, the height and permittivity of the dielectric substrate must be chosen correctly, for single-mode operation in the dielectric substrate. In the substrate is spread only TM wave.

The operational principle of the mushroom-like EBG structure can be explained by an LC equivalent circuit (see Fig. 6.4). The capacitance in this model results from the fringing electric field between the adjacent metallic patches. The inductance comes from the current flowing along adjacent patches and connecting vias. This equivalent

circuit model is able to predict the reflection phase as well as a part of surface wave properties. The equivalent circuit consisting of lumped elements is valid in evaluating the properties of the electromagnetic structures as long as the wavelength of interest is much longer than the dimensions of a unit cell. The capacitance inductances and inductance by the current on via in the equivalent circuit can be approximated by the following formulas [42], [45], [49], [50]:

$$C = \frac{(D - g) \cdot \epsilon_0 \cdot (1 + \epsilon_r)}{\pi} \cosh^{-1} \left( \frac{2(D - g) + g}{g} \right), \quad (6.2)$$

$$L = \mu_0 h, \quad (6.3)$$

$$f_r = \frac{1}{2\pi\sqrt{LC}}, \quad (6.4)$$

$$L_{via} = \frac{\mu_0}{2\pi} \left[ h \cdot \ln \left( \frac{h + \sqrt{R_{via}^2 + h^2}}{R_{via}} \right) + \frac{3}{2} \left( R_{via} - \sqrt{R_{via}^2 + h^2} \right) \right], \quad (6.5)$$

where  $h$  is thickness of the substrate,  $D$  is the lattice constant,  $g$  denotes the width of the gap, and  $\epsilon_r$  is relative permittivity of the substrate.

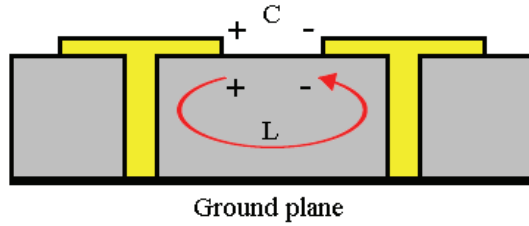


**Fig. 6.4:** LC equivalent circuit of the mushroom-like EBG structure.

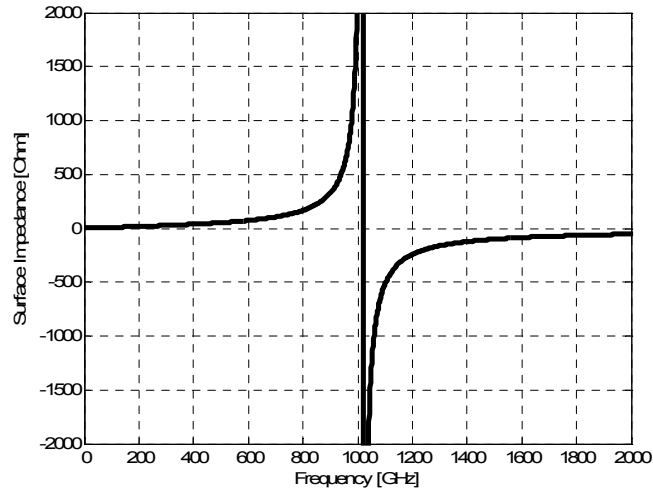


**Fig. 6.5:** The imaginary part of the surface impedance.

The surface impedance equals to the impedance of a parallel resonant circuit, consisting of the sheet capacitance and the sheet inductance and is defined by [42].

$$Z_{surface} = \frac{j\omega L}{1 + \omega^2 LC} \quad (6.6)$$

A typical surface impedance of a mushroom-like EBG structure is shown in Fig. 6.5. The surface impedance is inductive at low frequencies, and capacitive at high frequencies.

In-phase reflection characteristics of mushroom-like EBG structures are an important feature. Reflection phase can be calculated from the circuit model [42]:

$$\Phi = \text{Im} \left\{ \ln \left( \frac{Z_{surface} - 120\pi}{Z_{surface} + 120\pi} \right) \right\} \quad (6.7)$$

The reflection phase is  $180^\circ$  if a plane wave irradiates normally a perfectly electrically conductive plane. However, the phase of the electromagnetic wave reflected from EBG structures varies from  $-180^\circ$  to  $+180^\circ$  with frequency. A typical reflection phase of a mushroom-like EBG structure is shown in Fig. 6.6.

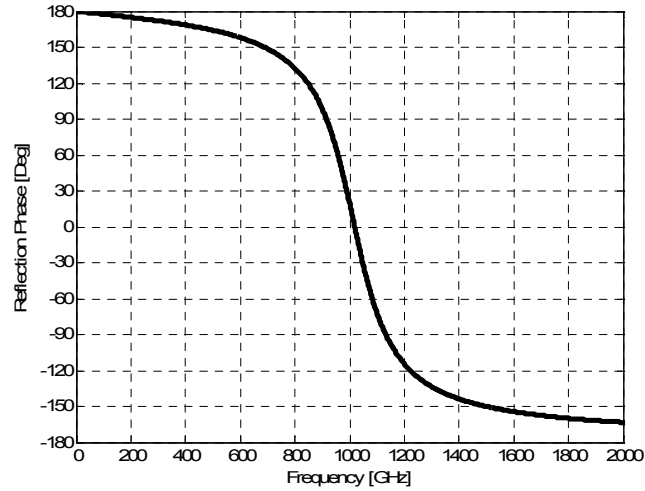


**Fig. 6.6:** Reflection phase calculated from LC equivalent circuit.

At the resonant frequency of the structure, the reflection phase is zero and the structure behaves like an artificial magnetic conductor (AMC). The reflection phase ranging from  $+90^\circ$  to  $-90^\circ$  informs us about the position of the forbidden zone (band gap) for TM waves. With the reflection phase ranging from  $+90^\circ$  to  $-90^\circ$ , the reflected wave interferes with the incident wave in. This in-phase reflection enables us to design low profile antennas [49].

The exact position of pass bands and band gaps in the frequency spectrum can be obtained from the dispersion relation of surface waves along the contour of the so-called irreducible Brillouin zone. A calculation procedure of the irreducible Brillouin zone is referred in [41], [42], [44]. The irreducible Brillouin zone for the 2D periodic structure with the square lattice is shown in Fig. 6.7. When computing the dispersion diagram, resonant frequencies of eigen-modes along the triangle with nodes marked  $\Gamma$ , X, M (symmetry points) are calculated.

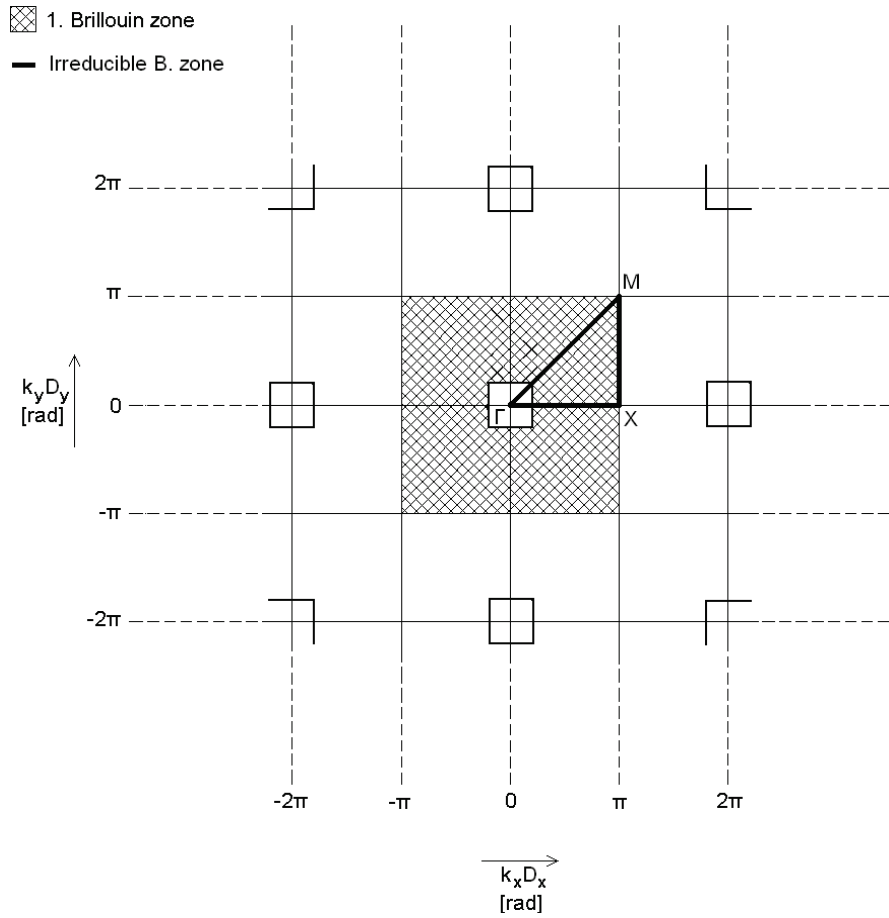


Fig. 6.7: The irreducible Brillouin zone [44].

A systematic calculation procedure of the dispersion diagram is referred in [44]. The example of the dispersion diagram for a lower frequency band is shown in Fig. 6.8. The surface wave band-gap is between 9.23 GHz and 10.70 GHz.

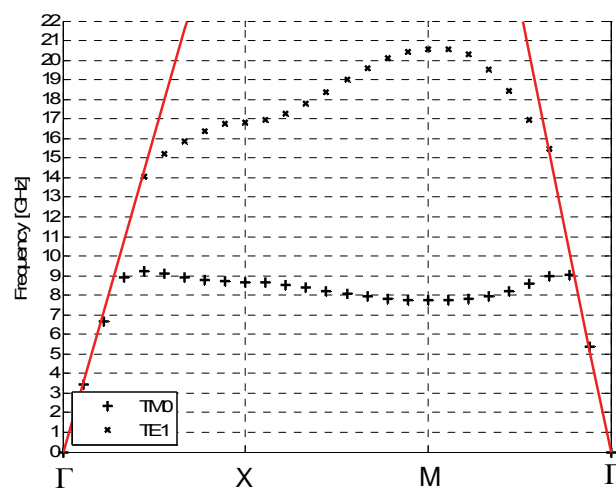


Fig. 6.8: Dispersion diagram of the mushroom-like EBG structure.

## 6.4 Verification of the design method

In order to verify the design method, an experimental structure was fabricated. The structure was analyzed by CST Microwave Studio (CST MWS). These experimental verifications are around  $f = 10$  GHz in order to verify the theoretical approach easily. The THz frequency band exhibits the same principle of surface waves propagation in a dielectric substrate as at so much lower frequencies band. Therefore, it is possible to use this method also in the THz frequency band. The Problems is an appropriate choice of substrates and high losses in the dielectric.

The unit cell of the mushroom-like EBG structure (Fig. 6.9) was of the following dimensions: the lattice constant  $D_{\text{EBG}} = 2.93$  mm, the width of the patch  $P_{\text{EBG}} = 2.633$  mm and the width of via  $R_{\text{EBG}} = 0.6$  mm. The metal patch with via hole is placed on the FR-4 substrate with relative permittivity  $\epsilon_r = 4.15$  and thickness  $h = 1.52$  mm.

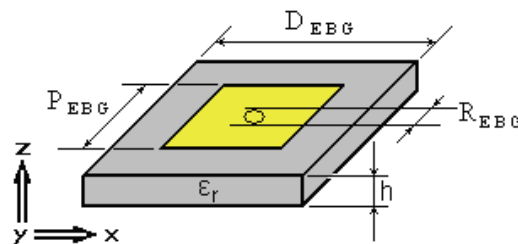


Fig. 6.9: The dimensions of the unit cell.

Figure 6.10 shows frequency response the reflection phase and surface wave transmission of the mushroom-like EBG structure computed by CST MWS. Obviously, the mushroom has a positive reflection phase  $\phi_1 = 84.78^\circ$ .

Figure 6.11 shows dispersion diagram of the mushroom-like EBG structure. The band-gap is from 10.00 GHz to 12.85 GHz. The operating frequency is  $f = 11$  GHz. The EBG consisting of  $20 \times 20$  unit cells was used for the experimental verification.

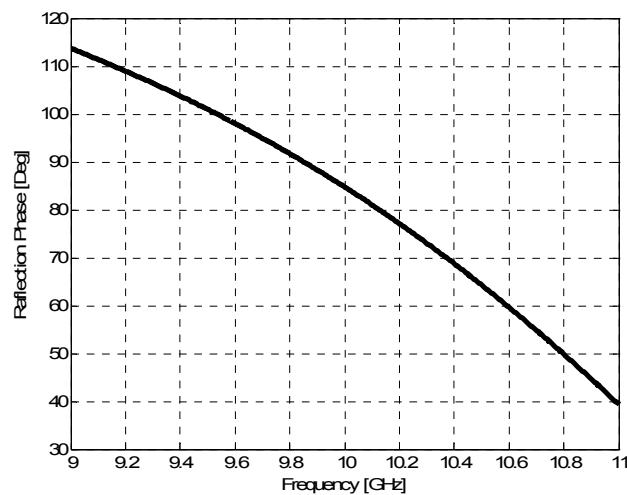
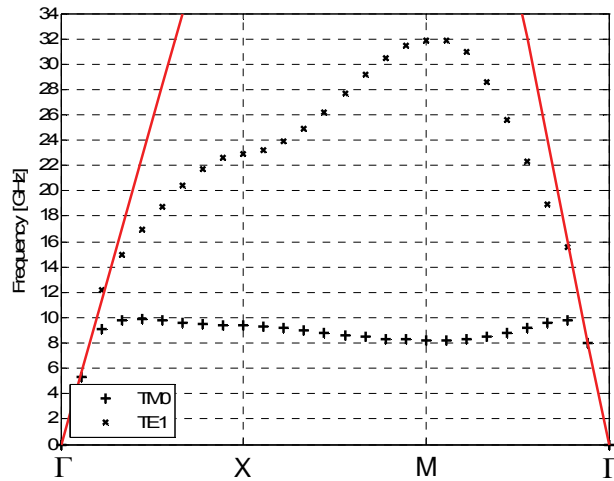
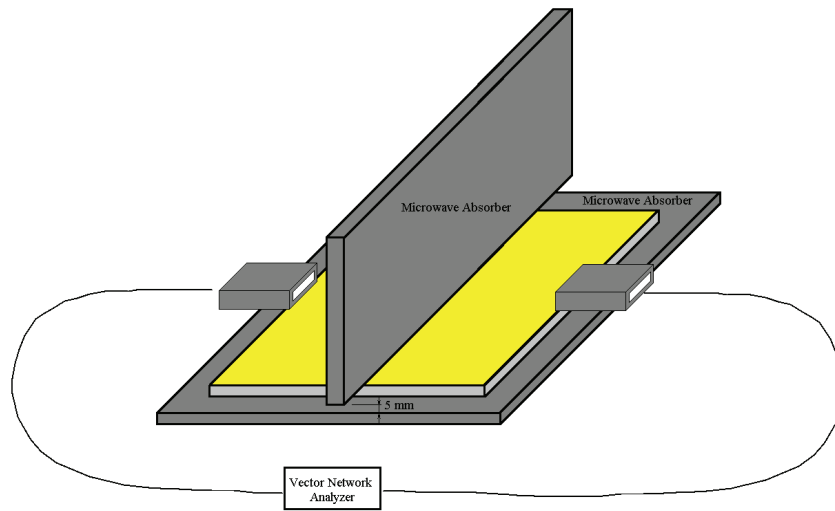


Fig. 6.10: Reflection phase response of the mushroom-like EBG structure.



**Fig. 6.11:** Dispersion diagram of the mushroom-like EBG structure

The transmission of electromagnetic waves over the mushroom-like EBG structure was measured using two identical open-waveguide antennas communicating via surface waves supported by the structure. The measurement setup for TM waves and TE waves is shown in Fig. 6.12. The results obtained for TM propagation are shown in Fig. 6.13.



**Fig. 6.12:** Experimental setup for measuring transmission via surface waves.

The mushroom-like EBG and the conventional metallic ground plane were investigated in the  $\Gamma$ -X direction. The surface impedance of the EBG board was inductive (at lower frequencies), and the EBG supported the propagation of TM surface waves. The TE surface waves were in cutoff. The surface impedance became capacitive with increasing frequency, the transmission magnitude of TM waves decreased and the transmission magnitude of TE wave increased.

Fig. 6.14 and Fig. 6.15 show the distribution of the electric field intensity (TM waves) and the magnetic field intensity (TE waves) over the mushroom-like EBG structure. These results are achieved by the analysis of a semi-infinite model [44]. The field distributions are shown for three frequencies:

- 09.00 GHz (TM waves propagate, TE waves are in cutoff),
- 10.00 GHz (both TM and TE waves are in cutoff),
- 15.00 GHz (TM waves are in cutoff, TE waves propagate).

The results confirm agreement between the dispersion analysis and the measurement.

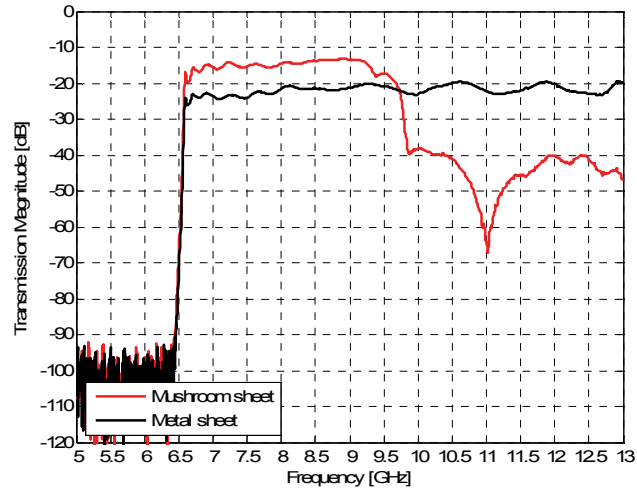


**Fig. 6.13:** Measured transmission of TM surface waves on mushroom-like EBG and metal sheet.

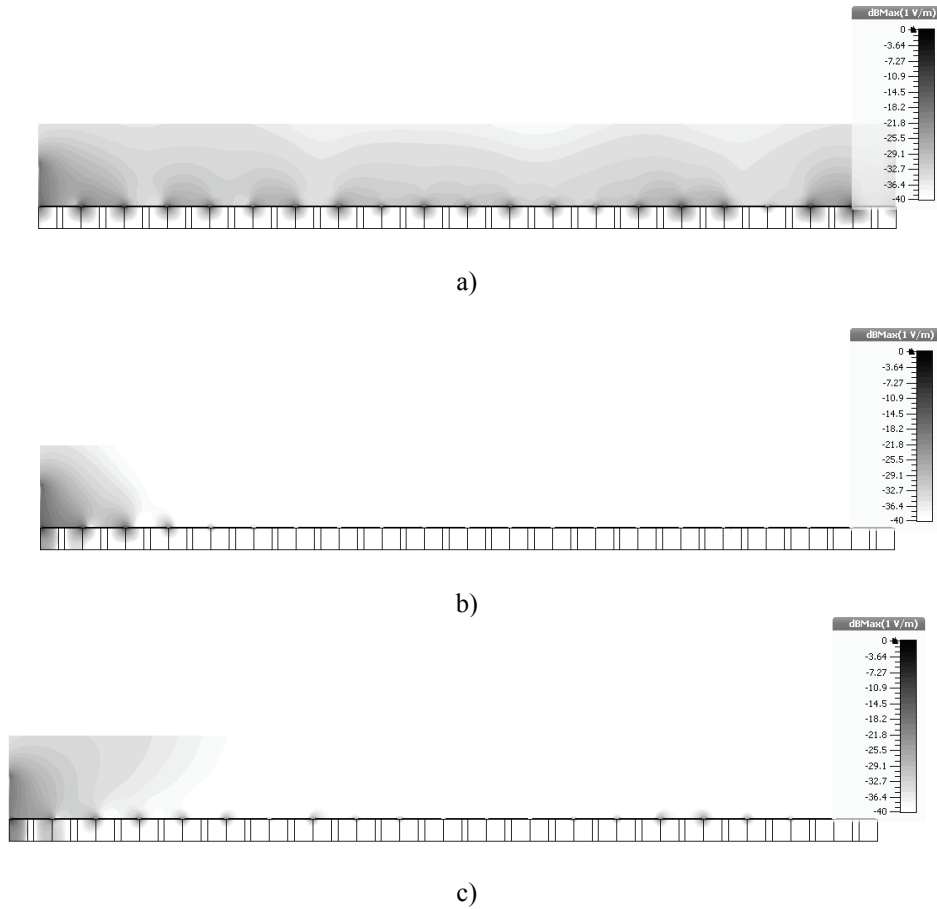


**Fig. 6.14:** TM surface wave propagation on mushroom-like EBG: a) 9 GHz, b) 10 GHz, c) 15 GHz.

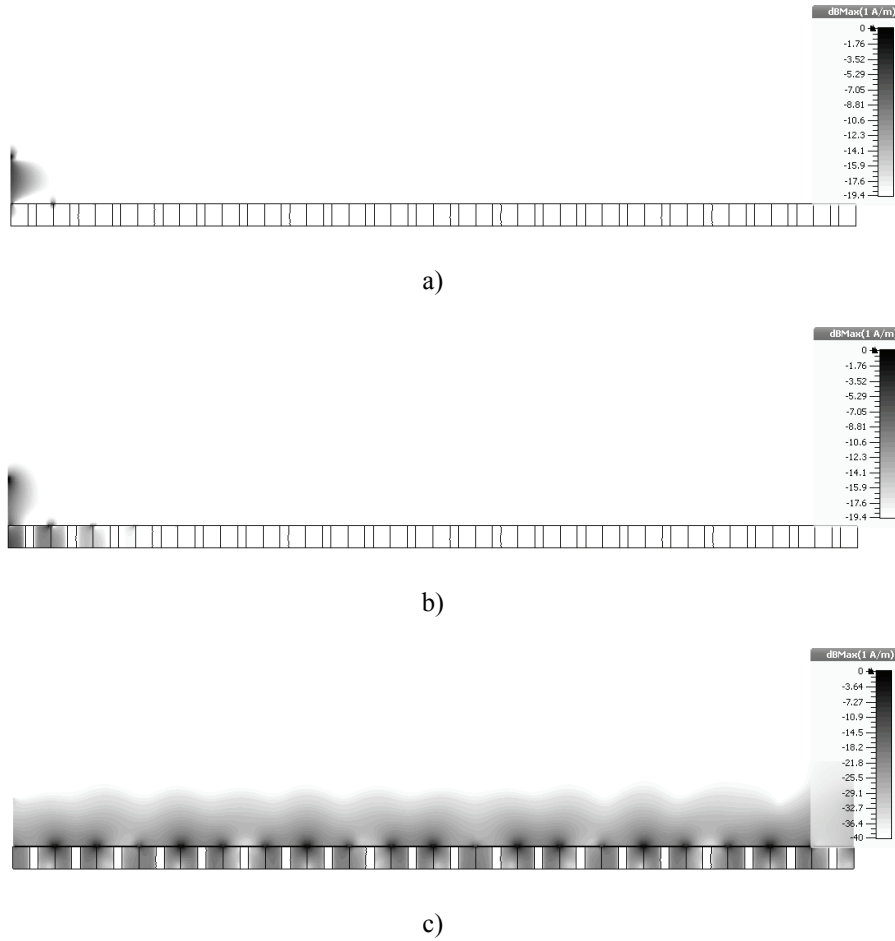
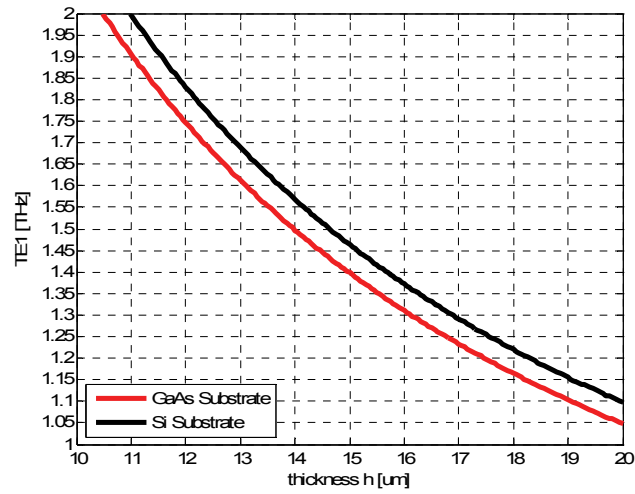


**Fig. 6.15:** TE surface wave propagation on mushroom-like EBG: a) 9 GHz, b) 10 GHz, c) 15 GHz.

## 6.5 THz mushroom-like EBG structure

If the dielectric substrate with permittivity  $\epsilon_r$  and thickness  $h$  is chosen properly, a single-mode operation in the dielectric substrate is achieved, and a TM wave will propagate there only. Results of the modal analysis are shown in Fig. 6.16 and described in Table 6.1.

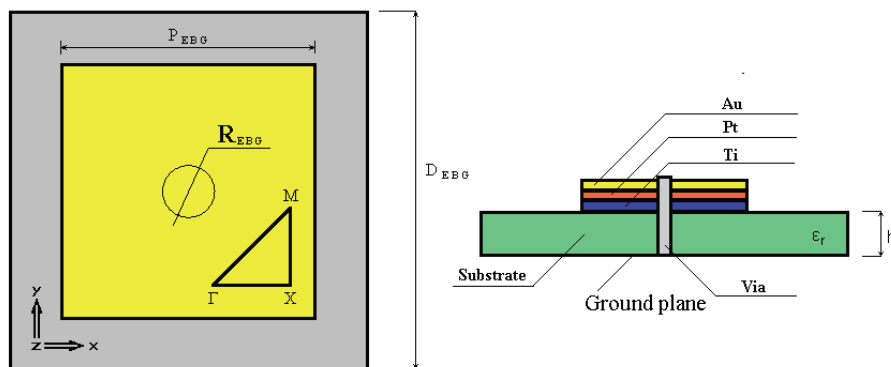
Dimensions of the unit cell of the mushroom-like EBG structure are shown in Fig. 6.17. The lattice constant is  $D_{\text{EBG}} = 35.08 \mu\text{m}$ , the width of the patch is  $P_{\text{EBG}} = 19.38 \mu\text{m}$  and the width of the via is  $R_{\text{EBG}} = 7 \mu\text{m}$ . The gold patch with the via hole is placed on the GaAs substrate with permittivity  $\epsilon_r = 12.94$  and thickness  $h = 15 \mu\text{m}$ . The loss tangent was assumed to be 0.006. All the metal traces consisted of titanium / platinum / gold layers (thicknesses: 30 nm / 40 nm / 200 nm) in the simulation.



**Fig. 6.16:** Modal analysis of GaAs substrate and Si substrate.

**Table 6.1:** Modal analysis of GaAs substrate and Si substrate.

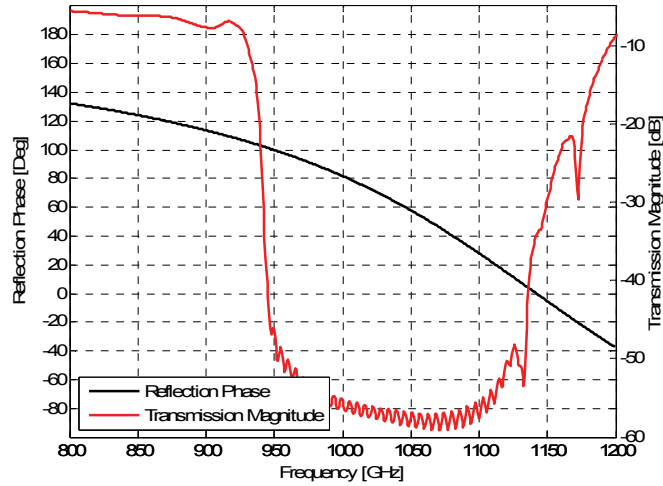
| $h$ [ $\mu\text{m}$ ] | TE <sub>1</sub> [THz] - GaAs | TE <sub>1</sub> [THz] - Si |
|-----------------------|------------------------------|----------------------------|
| 10                    | 2.096                        | 2.195                      |
| 11                    | 1.906                        | 1.996                      |
| 12                    | 1.747                        | 1.830                      |
| 13                    | 1.613                        | 1.689                      |
| 14                    | 1.497                        | 1.568                      |
| 15                    | 1.398                        | 1.464                      |
| 16                    | 1.310                        | 1.372                      |
| 17                    | 1.233                        | 1.291                      |
| 18                    | 1.165                        | 1.220                      |
| 19                    | 1.103                        | 1.156                      |
| 20                    | 1.048                        | 1.098                      |



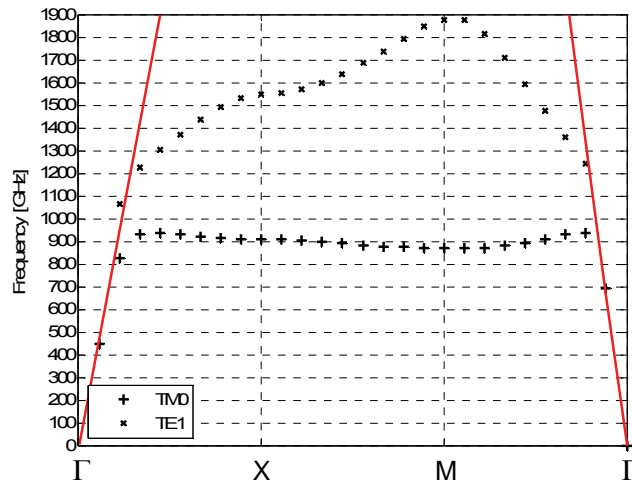
**Fig. 6.17:** The dimensions of the unit cell.

Fig. 6.18 shows the frequency response of the reflection phase of the mushroom-like EBG structure and the transmission of surface wave of this structure computed by CST MWS. Obviously, the EBG shows a positive reflection phase  $\phi_2 = 81.77^\circ$ .

Fig. 6.19 shows the dispersion diagram of the EBG. The surface wave band-gap is between 940 GHz and 1 200 GHz. The operating frequency of the CP THz cross slots patch antenna is  $f = 1$  THz.



**Fig. 6.18:** Frequency response of reflection phase and surface wave transmission of the EBG structure.



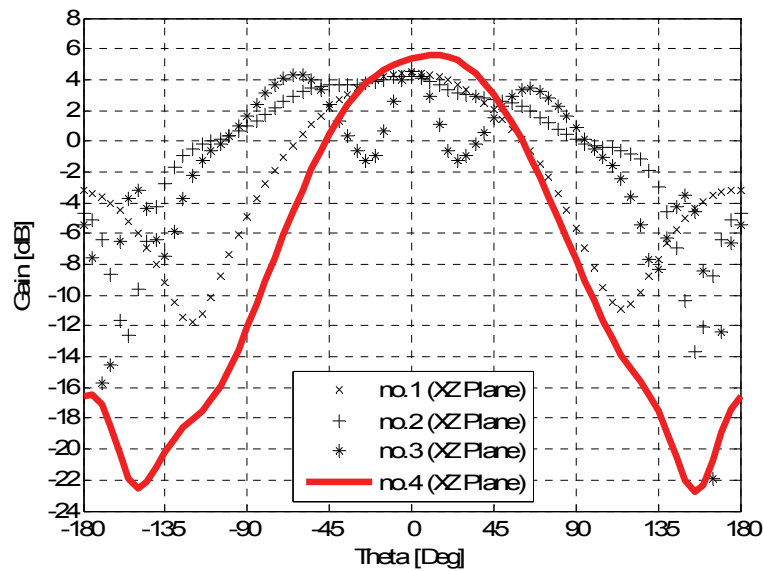
**Fig. 6.19:** Dispersion diagram of the mushroom-like EBG structure.

Let us investigate the influence of the mushroom-like EBG structure on antenna performance. For simplicity, the radiating element with linear polarization was used. The ground plane was implemented in four dimensions. The most important parameters are radiation patterns for each plane, side lobe level (SSL), front-to-back ratio (FBR), gain and radiation efficiency ( $\eta$ ) of the designed structure.

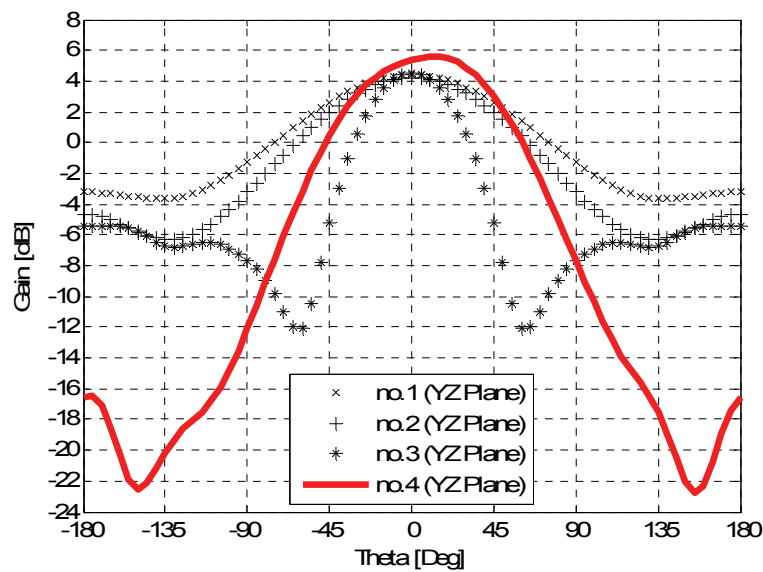
Following scenarios are considered:

- **No. 1:** Antenna element with ground plane  $100 \mu\text{m} \times 100 \mu\text{m}$  at  $f = 1 \text{ THz}$ ;
- **No. 2:** Antenna element with ground plane  $300 \mu\text{m} \times 300 \mu\text{m}$  at  $f = 1 \text{ THz}$ ;
- **No. 3:** Antenna element with ground plane  $600 \mu\text{m} \times 600 \mu\text{m}$  at  $f = 1 \text{ THz}$ ;
- **No. 4:** Antenna element with ground plane  $600 \mu\text{m} \times 600 \mu\text{m}$  at  $f = 1 \text{ THz}$  completed by a mushroom-like EBG structure consisting of  $18 \times 18$  unit cells.

The influence of the mushroom-like EBG structure on radiation patterns of the designed antenna is shown in Fig. 6.20 and obtained results are summarized in Table 6.2.



a)



b)

**Fig. 6.20:** Radiation pattern of a simple patch antenna, a) XZ plane, b) YZ plane.

**Table 6.2:** Simulation results for different configurations of EBG antennas.

| Scenario for $f = 1$ THz                                    | SSL (XZ plane) | SSL (YZ plane) | Gain   |
|---|----------------|----------------|--------|
| 100 $\mu\text{m} \times 100 \mu\text{m}$ ground plane       | -7.6 dB        | -7.7 dB        | 4.5 dB |
| 300 $\mu\text{m} \times 300 \mu\text{m}$ ground plane       | -8.9 dB        | -8.9 dB        | 4.4 dB |
| 600 $\mu\text{m} \times 600 \mu\text{m}$ ground plane       | -1.1 dB        | -9.9 dB        | 4.2 dB |
| 600 $\mu\text{m} \times 600 \mu\text{m}$ ground plane + EBG | -22.0 dB       | -22.0 dB       | 5.6 dB |

| Scenario for $f = 1$ THz                                    | FBR (XZ plane) | FBR (YZ plane) | $\mu$  |
|---|----------------|----------------|--------|
| 100 $\mu\text{m} \times 100 \mu\text{m}$ ground plane       | 7.65 dB        | 7.65 dB        | 84.1 % |
| 300 $\mu\text{m} \times 300 \mu\text{m}$ ground plane       | 8.64 dB        | 8.64 dB        | 84.3 % |
| 600 $\mu\text{m} \times 600 \mu\text{m}$ ground plane       | 10.71 dB       | 10.71 dB       | 84.5 % |
| 600 $\mu\text{m} \times 600 \mu\text{m}$ ground plane + EBG | 23.76 dB       | 23.76 dB       | 89.5 % |

The described effects correspond to the presented theory. The mushroom-like EBG structure supports smooth and almost symmetric radiation patterns, better side lobe level, better front-to-back ratio and lower cross-polarization. Moreover, the mutual coupling between radiating antennas is influenced as illustrated by Fig. 6.21.

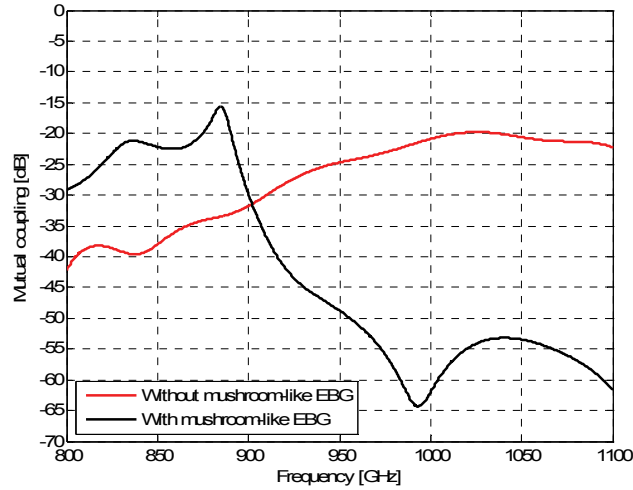


**Fig. 6.21:** Mutual coupling between two antenna radiators.

Figure 6.22 shows electric field distribution on the antenna surface and the antenna surface with mushroom-like EBG structure. Obviously, the mushroom-like EBG contributes to the suppression of surface waves and substantially improves the antenna performance.

Fig 6.23 shows that the spacing  $S$  between the antenna element and the surrounding mushroom-like EBG is crucial both from the viewpoint of impedance matching and radiation characteristics (shape of radiation pattern, gain of an antenna).

If  $S$  is small, the coupling between the radiating element and mushroom cells is strong, and the antenna cannot be tuned. Increasing  $S$ , the influence of EBG on radiation properties of the antenna weakens rapidly. This phenomenon is partially described in [51], but no particular recommendation for a correct choice of  $S$  is given there.

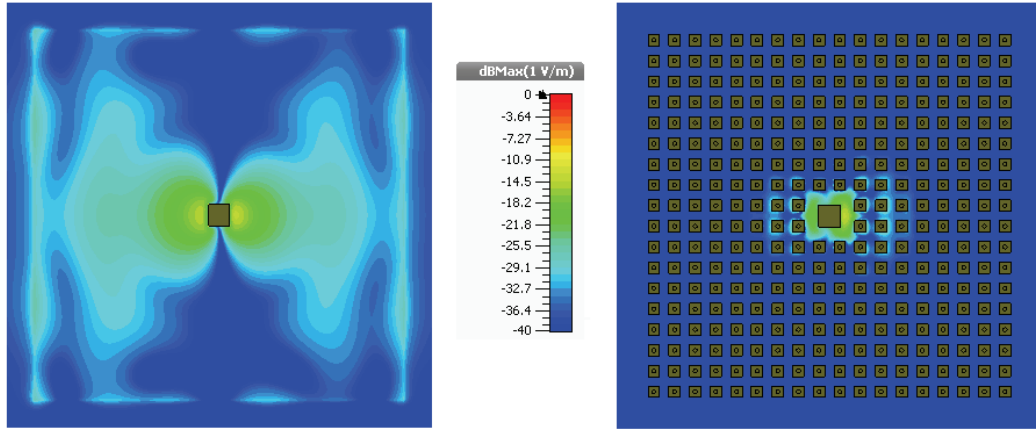


**Fig. 6.22:** Electric field distribution (z-component) on the antenna surface (left) and the antenna surface with mushroom-like EBG structure (right).

Considering a plane wave irradiating the designed mushroom-like EBG structure from the angle close to  $90^\circ$  (almost surface wave), the response of the reflection phase is approximately  $0^\circ$ . The interference between the direct wave radiated by the antenna and waves reflected from the mushroom-like EBG is then constructive if the gap between the patch and the mushroom is approximately half of the wavelength,  $S \approx \lambda_g/2$  [52]. The minimal number of unit cells of the EBG is three units in one direction (for suppressing surface waves).

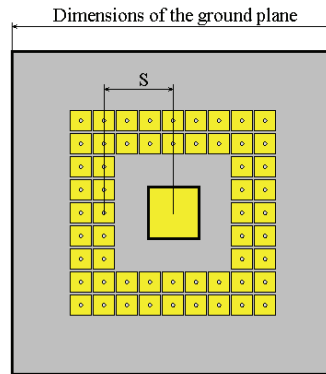


**Fig. 6.23:** The spacing S between the antenna element and the surrounding mushroom-like EBG.

## 6.6 THz superstrates

A reflective surface can be used as a superstrate covering the antenna. Thanks to the multiple reflections between the reflective superstrate and the antenna ground plane, the gain of the antenna can be significantly enhanced. The structure is similar to the Fabry-Perot resonator.

Using a ray-tracing method, a simple formula can be derived [54] relating the reflection magnitude of the superstrate and the relative increase of the antenna directivity. The ground plane and the reflective surface (PRS, Superstrate) form a resonant cavity; see Fig. 6.24 [43].

Antennas with the reflective superstrate excel in high directivity, low profile and

simple configuration. The superstrate is placed half wavelength above the ground plane approximately. The superstrate is usually implemented as a planar periodic structure (similar to frequency selective surfaces, FSS). Shaping the superstrate into a cylinder and using an antenna radiator on a cylindrical ground plane, we can create an antenna with a broad beam width in the azimuthal plane and a narrow beam width in the elevation plane [54].

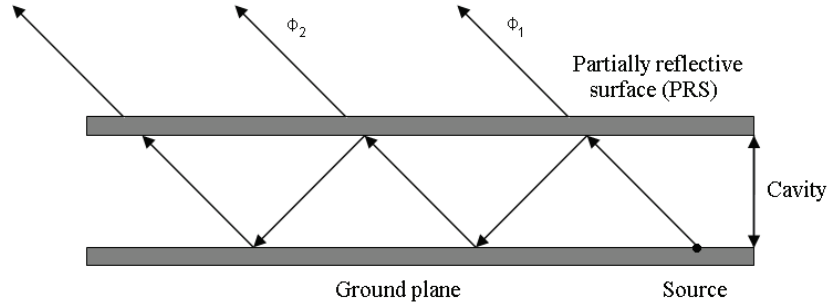


**Fig. 6.24:** The principle of the Fabry-Perot resonator.

EBG resonator antennas usually employ volumetric periodic dielectric structures. PRS antennas use planar periodic metallic structures printed on a substrate. PRS antennas tend to have a lower profile than EBG antennas. Unfortunately, low radiation bandwidth due to a high Q factor of the resonating structure belongs to disadvantages of both PRS antennas and EBG ones.

Phase shifts are introduced by the path length, the ground plane and the phase of the reflection coefficient of the PRS. The transmitted power can be derived by considering the interference of waves partially transmitted through the PRS. The directivity of the cavity at the bore-sight can be expressed as the ratio of the transmitted power  $P_T$  to the power of the source  $P_S$  [43]

$$D = \frac{P_T}{P_S} = \frac{1 - R^2}{1 + R^2 - 2R \cos(\Delta\Phi)} \quad (6.8)$$

where  $R e^{j\Phi_R}$  is the complex reflection coefficient of the PRS and  $\Delta\Phi = \phi_2 - \phi_1$  (see Fig. 6.24). The resonance condition is satisfied if the phase difference of the transmitted waves equals zero [43]:

$$\Delta\Phi = \Phi_R - \pi - \frac{2\pi}{\lambda} \cdot 2 \cdot h_{cavity} = 2\pi N, \quad N = 0, 1, 2.. \quad (6.9)$$

Thus

$$h_{cavity} = \left( \frac{\Phi_R - 1}{\pi} \right) \frac{\lambda}{4} + \frac{\lambda}{2} \cdot N \quad (6.10)$$

In (6.9) and (6.10),  $\lambda$  is the free-space wavelength. At the resonance, the maximum bore-sight directivity (dB) can be obtained [43]:

$$D = 10 \cdot \log \left( \frac{1 + R}{1 - R} \right) \quad (6.11)$$

The directivity of the cavity is obviously determined by the reflection properties of the

PRS. The reflection phase of a highly reflective surface approaches  $\pi$ , and the height of the resonant cavity should be close to  $\lambda/2$ . For such a cavity, the directivity (6.11) is very high since  $R$  approaches the ideal value 1 [55].

The superstrate can be purely dielectric, purely metallic or metallo-dielectric. One-dimensional dielectric EBG containing a defect resonator is the basic type of the superstrate. The defect causes an extremely sharp pass band lying inside the stop band.

## 6.7 THz planar lenses

The unit cell of a partially reflective surface (PRS, superstrate) is shown in Fig. 6.25. The unit cell is of following dimensions:  $D_{\text{super}} = 154.94 \mu\text{m}$ ,  $P_{\text{super}} = 144.95 \mu\text{m}$ ,  $\epsilon_r = 11.9$  and  $h_{\text{super}} = 3 \mu\text{m}$ . Here, we use higher dielectrics to achieve a high-reflecting superstrate. The superstrate was designed for the operating frequency  $f = 1 \text{ THz}$ . The antenna structure consists of a superstrate on the top and a simple radiator.

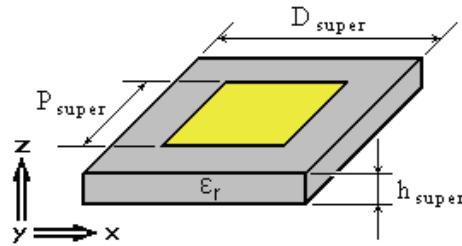


Fig. 6.25: Dimensions of the PRS unit cell.

The gain of the antenna with the superstrate is determined by lateral dimensions of the surface of the superstrate, the reflection coefficient of the superstrate and the gain of the radiator. This antenna radiates energy to the cavity formed by the superstrate and the ground plane. The principle of the superstrate antenna is explained in Fig. 6.26.

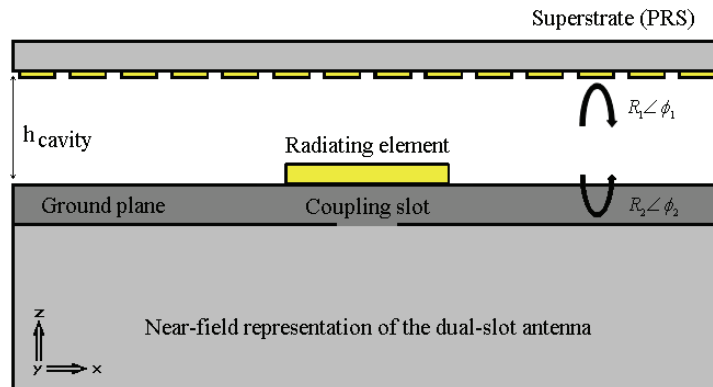
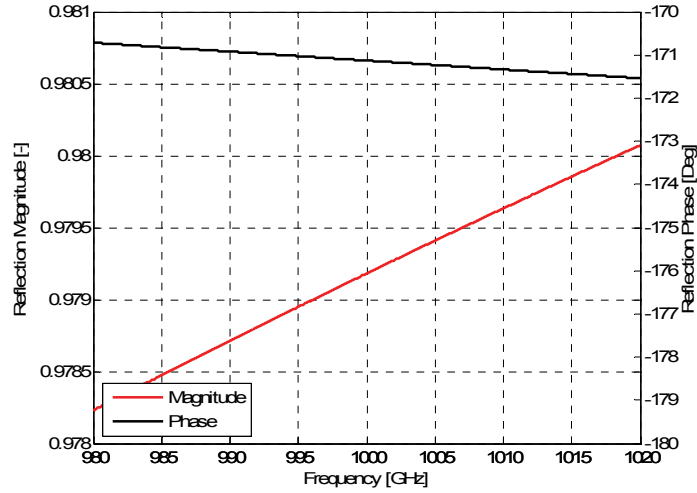


Fig. 6.26: Schematic of the superstrate antenna.

The superstrate with the reflection coefficient  $R_1 \angle \phi_1$  is placed in the distance  $h_{\text{cavity}}$  above the ground plane. The reflection coefficient of the ground plane is  $R_2 \angle \phi_2$ .

Both reflection coefficients  $R_1 \angle \phi_1$  and  $R_2 \angle \phi_2$  are functions of the angle of incidence. For simplified ray analysis [55], we consider normal incidence only.

Reflection properties of the designed superstrate were computed by CST MWS. Frequency response of complex reflection coefficient of the superstrate is shown in Figure 6.27.



**Fig. 6.27:** Frequency response of the complex reflection coefficient of the superstrate.

The transmission magnitude is influenced by the defect in the periodic structure, which causes an extremely sharp pass band lying inside the stop band (Fig. 6.28).

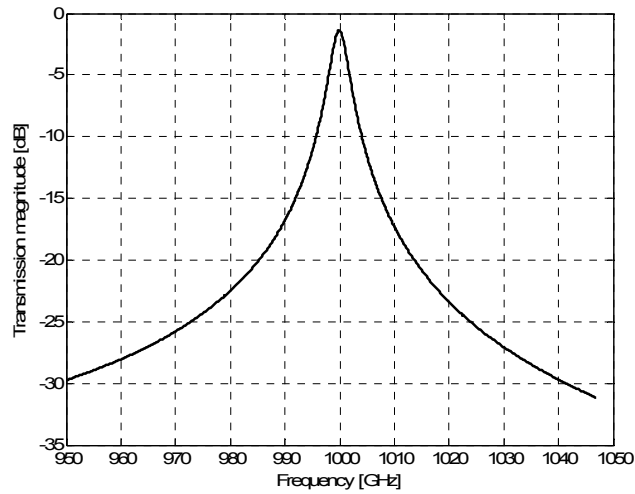


**Fig. 6.28:** Frequency dependence of the transmission magnitude of the superstrate.

Obviously, the reflection coefficient of the superstrate has a phase  $\phi_1 = -171.13^\circ$  and a magnitude  $R_1 = 0.979$  at the operating frequency. The theoretical value of the gain is  $G = 19.74$  dB. So, the height of the resonant cavity  $h_{cavity}$  is determined by the reflection phase of the superstrate  $\phi_1$ , the reflection phase of the ground plane  $\phi_2$  and the operating wavelength  $\lambda$ :

$$h_{cavity} = \left( \frac{\phi_1 + \phi_2}{\pi} \right) \frac{\lambda}{4} + \frac{\lambda}{2}. \quad (6.12)$$

According to the above condition, the maximum power  $S_{\max}$  in the forward direction can be obtained as:

$$S_{\max} = \frac{1+\rho}{1-\rho} S_0 \quad (6.13)$$

Here,  $S_0$  corresponds to the forward power from the source without superstrate. If the condition (6.12) is satisfied, the higher the reflection coefficient  $\rho$  is, the higher the forward power  $S_{\max}$  is. The reflection phases are very close to  $\phi_1 = \phi_2 = \pi$ , and the distance  $h_{\text{cavity}}$  between the ground plane and the superstrate should be  $\lambda/2$  at the operating frequency, but the actual value is  $h_{\text{cavity}} = 152.81 \mu\text{m}$

The superstrate consists of  $6 \times 6$  cells. The dimensions of the designed structure are  $1000 \mu\text{m} \times 1000 \mu\text{m}$ . Influence of the superstrate on radiation patterns of the designed antenna is shown in Fig. 6.29 and obtained results are summarized in Table 6.3. The figures 6.29a and 6.29b document the disintegration of radiation patterns in the main direction. In this case, dimensions of the ground plane are  $1000 \mu\text{m} \times 1000 \mu\text{m}$  and dimensions of the radiating element are  $34.29 \mu\text{m} \times 34.29 \mu\text{m}$ .

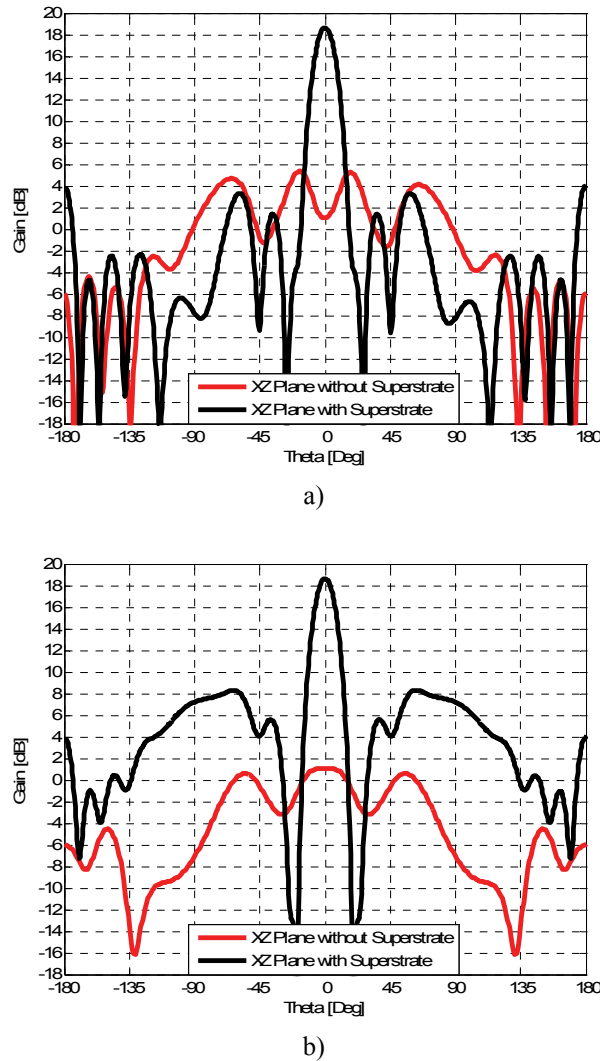


**Fig. 6.29:** Radiation patterns of the designed antenna with superstrate: a) XZ plane, b) YZ plane

Radiation patterns (Fig. 6.29) show significant changes in the radiation behavior of the antenna with the superstrate in comparison with a simple antenna. The antenna with superstrate excels in low side-lobe level and a considerable improvement of gain  $G_{\text{improve}} = 13.3$  dB. Fig. 6.30 shows the calculated gain improvement of the designed antenna.

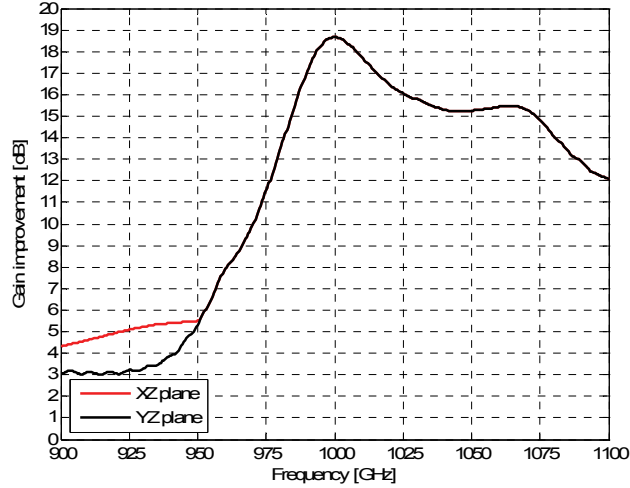


**Fig. 6.30:** Calculated gain improvement of the designed antenna.

**Table 6.3:** Simulation results for simple antenna and antenna with superstrate.

| Results for $f = 1$ THz, cavity = $\lambda/2$ | Simple antenna | Antenna with superstrate |
|---|----------------|--------------------------|
| SSL, XZ plane                                 | -1.3 dB        | -14.7 dB                 |
| SSL, YZ plane                                 | -5.6 dB        | -10.4 dB                 |
| FBR, XZ plane                                 | 7.0 dB         | 14.7 dB                  |
| FBR, YZ plane                                 | 7.0 dB         | 14.7 dB                  |
| Main lobe width, XZ plane                     | 162.2°         | 14.6°                    |
| Main lobe width, YZ plane                     | 43.9°          | 14.6°                    |
| Gain, XZ plane                                | 5.4 dB         | 18.7 dB                  |
| Gain, YZ plane                                | 1.2 dB         | 18.7 dB                  |
| Gain improvement                              | 0.0 dB         | 13.3 dB                  |

## 6.8 Reducing height of resonant cavity

The height of a Fabry-Perot resonator antenna is  $\lambda/2$  at the operating frequency. In order to decrease the height, the reflection phase of the ground plane or the superstrate has to be changed.

Papers [53], [56] describe exploitation of an artificial magnetic conductor (AMC) as a ground plane of the antenna. AMC can be implemented as a mushroom-like periodic structure. AMC reflects incident waves with a phase close to zero. The reflection phase of AMC approaches zero just at single frequency (a single resonant mode).

The bandwidth of AMC is limited by  $\pm 90^\circ$  phase shift of the reflection coefficient appearing after the increase / the decrease of frequency from the central one. If this condition is met, phase values cannot cause destructive interference between the direct wave and reflected waves [53].

The difference between the partially reflective surface with a conventional ground plane and an AMC one is shown in Fig. 6.31.

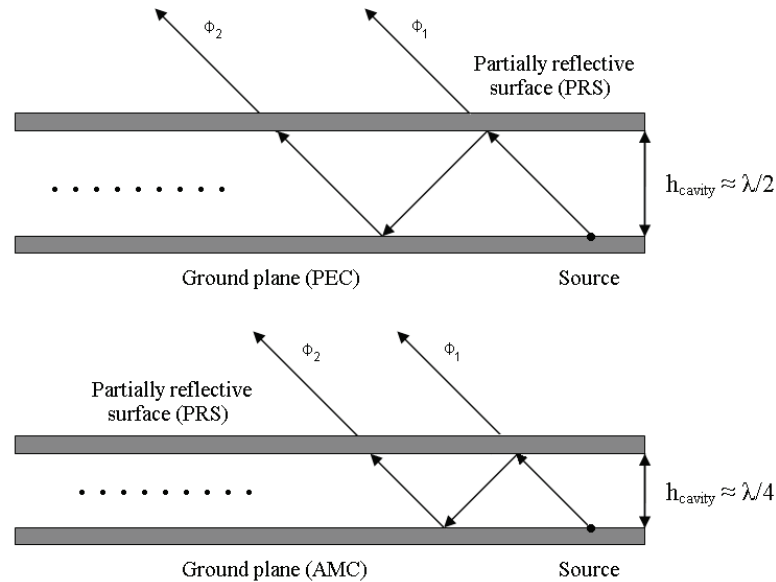


**Fig. 6.31:** Resonant cavity formed by PEC and PRS (top), and AMC and PRS (bottom).

Due to finite dimensions of the superstrate and the ground plane, real antennas suffer from a large backward radiation. That way, a significant amount of power is wasted in the backward hemisphere.

The thesis is aimed to replace the silicone lens by a planar lens. In the next subchapter, we replace the conventional superstrate of the resonator antenna by an LC superstrate. The designed LC superstrate exhibits negative reflection phase and high reflectivity. The mushroom-like RĒBG structure suppresses the propagation of surface waves and ensures the in-phase reflection coefficient.

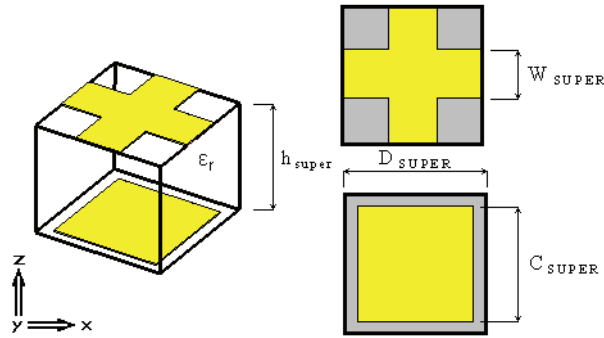
## 6.9 THz LC superstrate like planar lens

The LC superstrate is created by a double inductive and capacitive grid. The superstrate allows us to obtain a phase shift of the reflection coefficient in between  $+180^\circ$  and  $-180^\circ$ . We can control the thickness of the cavity in the range between  $\lambda/2$  to  $\lambda/300$ .

The unit cell of the LC superstrate is shown in Fig. 6.32. The unit cell of the superstrate is placed on the GaAs substrate with  $\epsilon_r = 12.98$  and  $h_{\text{super}} = 15 \mu\text{m}$  (the height is high to have a high reflectiveness).

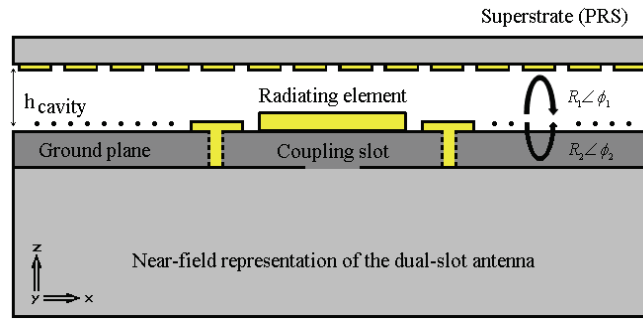
A capacitive metallic square patch is milled on one face and an inductive metallic mesh on another face of the substrate. The width of the inductive grid is

$W_{\text{super}} = 6.30 \mu\text{m}$ , and the width of the capacitive patch is  $C_{\text{super}} = 14.64 \mu\text{m}$ . Both the inductive grids and the capacitive patches have periodicity  $D_{\text{super}} = 17.97 \mu\text{m}$ .



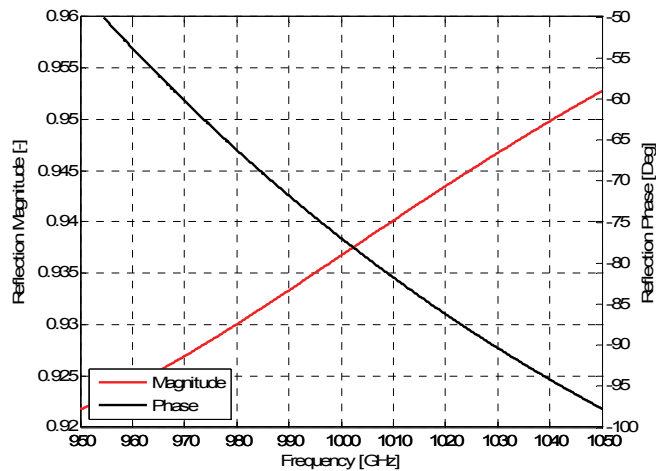
**Fig. 6.32:** Dimensions of the PRS unit cell.

The gain of the superstrate antenna is given by lateral dimensions of surfaces, the reflection coefficient of the superstrate and the gain of the antenna radiator. The antenna radiates energy to the cavity formed by the superstrate and the ground plane. The operating principle of the superstrate antenna is shown in Fig. 6.33.



**Fig. 6.33:** Schematic of the superstrate antenna.

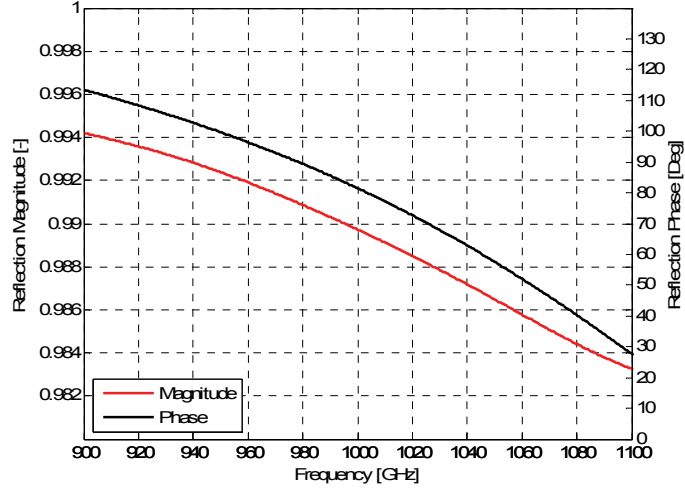
Reflection properties of the designed LC superstrate were computed by CST MWS. Fig. 6.34 shows the complex reflection coefficient of the LC superstrate. The LC superstrate layer has the negative reflection phase  $\phi_1 = -76.92^\circ$



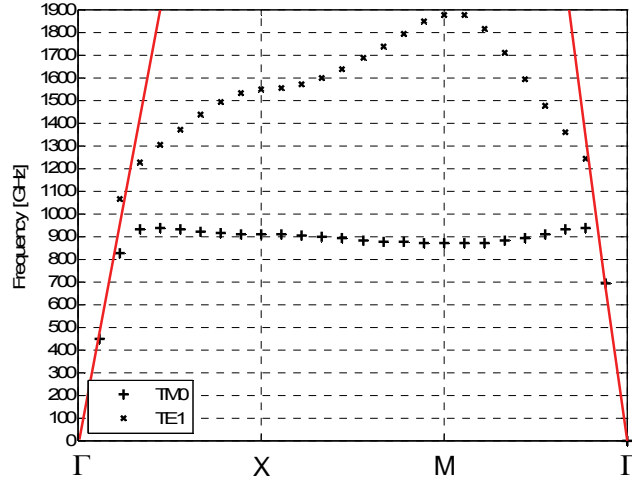
**Fig. 6.34:** Frequency response of the complex reflection coefficient of the LC superstrate.

Fig. 6.35 shows the complex reflection coefficient of the mushroom-like EBG structure computed by CST MWS. Obviously, the mushroom-like EBG structure has a positive reflection phase  $\phi_2 = 81.5^\circ$ .

Fig. 6.36 shows the dispersion diagram of the mushroom structure. The band-gap is between 940 and 1 200 GHz (Fig. 6.36). An operating frequency is  $f = 1$  THz. The mushroom-like EBG consisted of  $17 \times 17$  unit cells.



**Fig. 6.35:** Frequency response of complex reflection coefficient of the mushroom-like EBG.



**Fig. 6.36:** Dispersion diagram of the mushroom-like EBG structure.

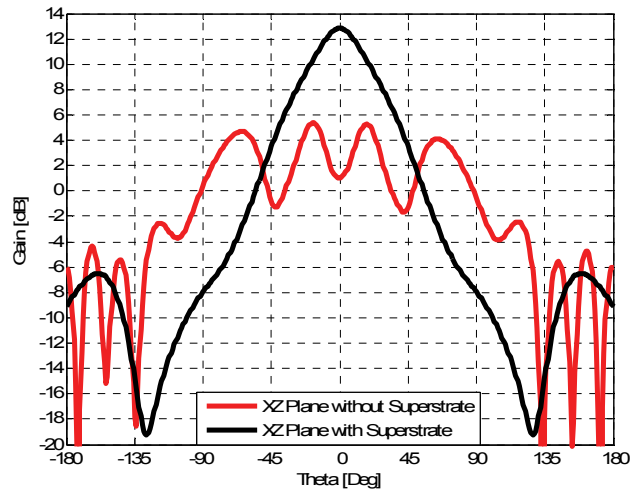
Obviously, the LC superstrate has a negative reflection phase  $\phi_1 = -76.92^\circ$  and a high magnitude of the reflection coefficient  $R = 0.936$  at the operating frequency. Using (6.11), we can obtain the gain  $G = 14.80$  dB. The maximal theoretical gain for the magnitude of the reflection coefficient  $R = 0.99$  is  $G_{\text{theoretical}} = 23$  dB. According to the Fabry-Perot resonance condition, we get

$$h_{\text{cavity}} = \frac{\lambda}{4\pi} (\phi_1 + \phi_2) + \frac{N\lambda}{2}, \quad (6.14)$$

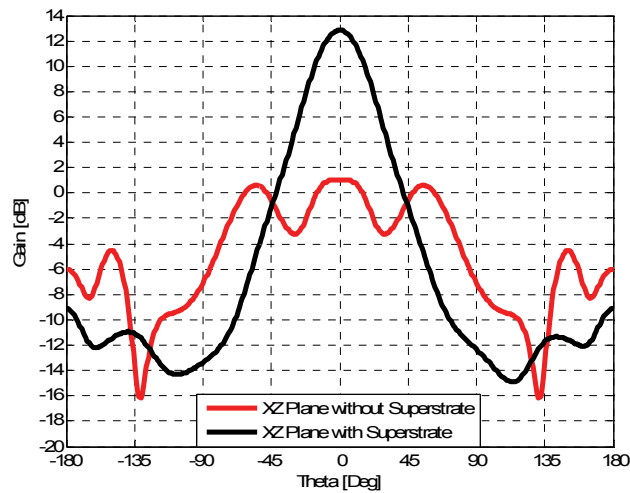
where  $N = 0$ ,  $\lambda$  is the free-space resonant wavelength,  $\phi_1$  is the reflection phase of the LC superstrate,  $\phi_2$  is the reflection phase of the mushroom-like EBG structure.

The Fabry-Perot resonator antenna excels in high-gain and low-profile antenna. The height of the cavity with the superstrate is  $h_{\text{cavity}} = 2 \mu\text{m}$  ( $\lambda/150$ ).

The LC superstrate consisting of  $35 \times 35$  cells, and the mushroom-like EBG structure consisting of  $18 \times 18$  cells were used. The dimensions of the proposed structure are  $629 \mu\text{m} \times 629 \mu\text{m}$ . The influence of the superstrate on radiation patterns of the designed antenna is shown in Fig. 6.37. The obtained results are summarized in Tables 6.4 and 6.5. Figure 6.38 shows the improvement of the gain of the antenna.



a)



b)

**Fig. 6.37:** Radiation pattern of the designed antenna with LC superstrate, a) XZ plane, b) YZ plane.

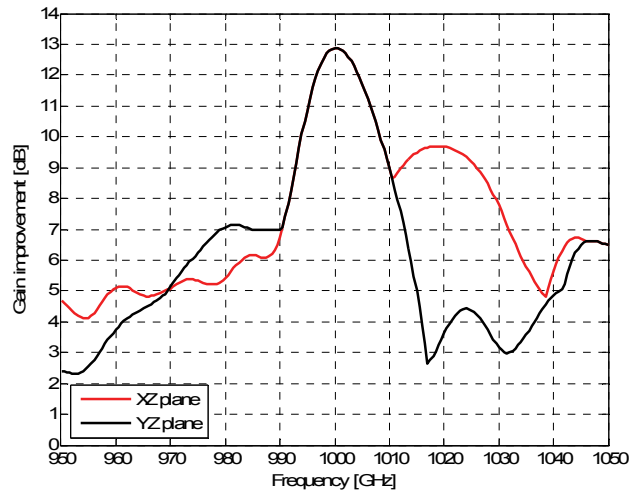


**Fig. 6.38:** Calculated improvement of the gain of the designed antenna.

**Table 6.4:** Simulation results for antenna with LC superstrate.

| Results for $f = 1$ THz, cavity = $\lambda/150$ | Simple antenna | Antenna with LC superstrate |
|---|----------------|-----------------------------|
| SSL, XZ plane                                   | -1.3 dB        | -22.0 dB                    |
| SSL, YZ plane                                   | -5.6 dB        | -19.3 dB                    |
| FBR, XZ plane                                   | 7.0 dB         | 22.0 dB                     |
| FBR, YZ plane                                   | 7.0 dB         | 18.5 dB                     |
| Main lobe width, XZ plane                       | 162.2°         | 33.8°                       |
| Main lobe width, YZ plane                       | 43.9°          | 40.7°                       |
| Gain, XZ plane                                  | 5.4 dB         | 13.0 dB                     |
| Gain, YZ plane                                  | 1.2 dB         | 13.0 dB                     |
| Gain improvement                                | 0.0 dB         | 7.6 dB                      |

**Table 6.5:** Comparison of different types of superstrates.

| Results for $f = 1$ THz   | Simple antenna | Antenna with superstrate | Antenna with LC superstrate |
|---------------------------|----------------|--------------------------|-----------------------------|
| SSL, XZ plane             | -1.3 dB        | -14.7 dB                 | -22.0 dB                    |
| SSL, YZ plane             | -5.6 dB        | -10.4 dB                 | -19.3 dB                    |
| FBR, XZ plane             | 7.0 dB         | 14.7 dB                  | 22.0 dB                     |
| FBR, YZ plane             | 7.0 dB         | 14.7 dB                  | 18.5 dB                     |
| Main lobe width, XZ plane | 162.2°         | 14.6°                    | 33.8°                       |
| Main lobe width, YZ plane | 43.9°          | 14.6°                    | 40.7°                       |
| Gain, XZ plane            | 5.4 dB         | 18.7 dB                  | 13.0 dB                     |
| Gain, YZ plane            | 1.2 dB         | 18.7 dB                  | 13.0 dB                     |
| Gain improvement          | 0.0 dB         | 13.3 dB                  | 7.6 dB                      |
| Cavity height             | none           | $\lambda/2$              | $\lambda/150$               |

## 6.10 Summary

In this section, we presented the practical application of the mushroom-like EBG structure for the suppression of surface waves in-phase reflection, improve mutual coupling between antennas, which brings benefit in antenna array, and electromagnetic energy focusing. Conclusions were verified by simulations in CST MWS and partly measurements.

We discussed ways of decreasing the height of the resonant cavity.

Disadvantages and advantages of the exploitation of periodic structures were analyzed. Antenna structure with the traditional superstrate was published in [37]. At present, we prepare a paper describing an antenna with the LC superstrate.

## 7 FINAL THZ ANTENNA

In this chapter, we present the final antenna configuration which comprises the THz source, the CP THz cross-slot patch antenna, the mushroom-like EBG structure and the LC superstrate. Functionality of the final structure is experimentally verified.

### 7.1 Circularly polarized THz antenna

The structure of the antenna is shown in Fig. 7.1. Dimensions of the antenna are summarized in Table 7.1. The designed antenna is composed of four building blocks:

- The THz source: the dual slot antenna (subchapter 5.4);
- The CP THz cross-slot patch antenna (subchapter 5.6);
- The THz mushroom-like EBG structure (subchapter 6.5);
- The THz LC superstrate cover (subchapter 6.9).

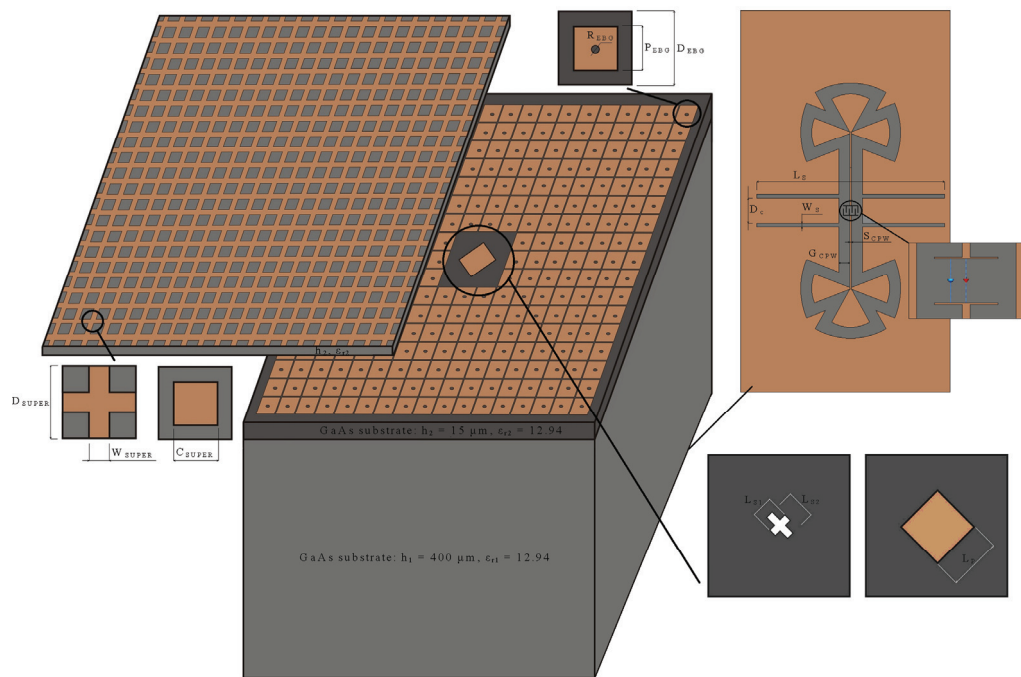
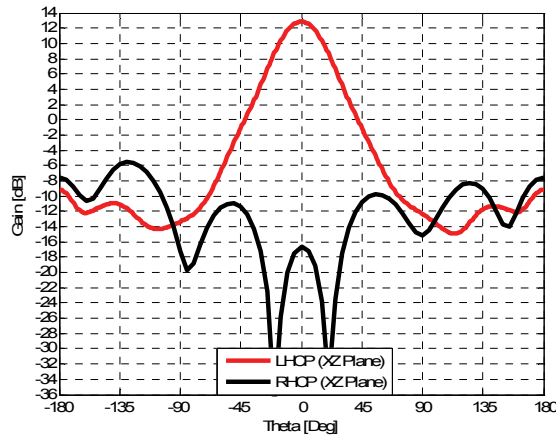


**Fig. 7.1:** The final THz antenna.

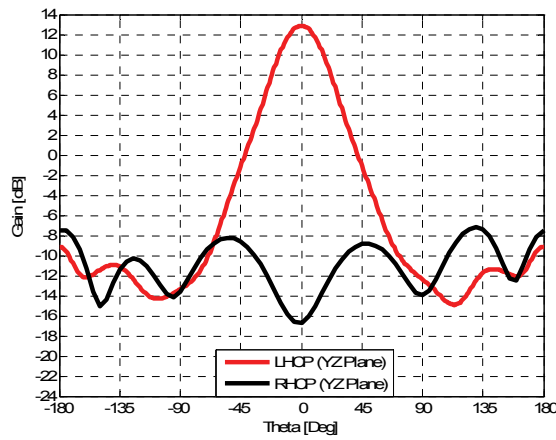
**Table 7.1:** Dimensions of the designed antenna.

| Parameters      | Value [ $\mu\text{m}$ ] | Parameters          | Value [ $\mu\text{m}$ ] |
|-----------------|-------------------------|---------------------|-------------------------|
| $h_1$           | 400.00                  | $G_{\text{CPW}}$    | 6.00                    |
| $\epsilon_{r1}$ | 12.94                   | $S_{\text{CPW}}$    | 1.00                    |
| $h_2$           | 15.00                   | $D_{\text{EBG}}$    | 35.08                   |
| $\epsilon_{r2}$ | 12.94                   | $P_{\text{EBG}}$    | 19.38                   |
| $L_{S1}$        | 23.24                   | $R_{\text{EBG}}$    | 7.00                    |
| $L_{S2}$        | 42.45                   | $D_{\text{SUPER}}$  | 17.97                   |
| $L_P$           | 31.98                   | $C_{\text{SUPER}}$  | 14.64                   |
| $L_S$           | 103.00                  | $W_{\text{SUPER}}$  | 6.30                    |
| $W_S$           | 2.00                    | $h_{\text{cavity}}$ | 2.00                    |
| $D_C$           | 13.76                   | $Z_{\text{port}}$   | 10 k $\Omega$           |

Fig. 7.2 shows simulated radiation patterns of the final antenna structure. In Fig. 7.3, axial ratio of the final antenna is depicted. Simulations in CST MWS show that the axial ratio bandwidth is 1.42 %. The final antenna generates left-handed circular polarization (LHCP).



a)



b)

**Fig. 7.2:** Radiation pattern of the final antenna, a) XZ plane, b) YZ plane.

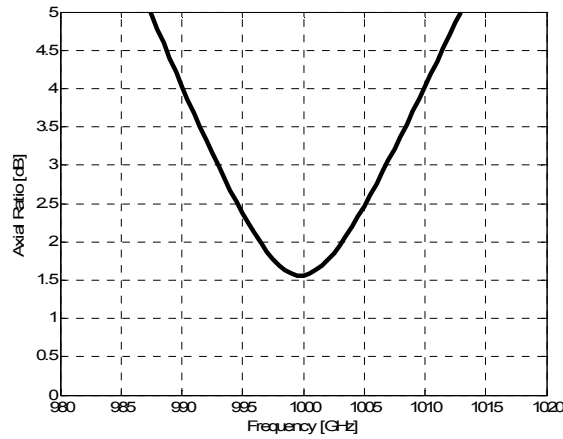


**Fig. 7.3:** Axial ratio in broadside direction of the final antenna.

Fig. 7.4 shows the calculated gain improvement of the final antenna. The results are summarized in the Table 7.2.

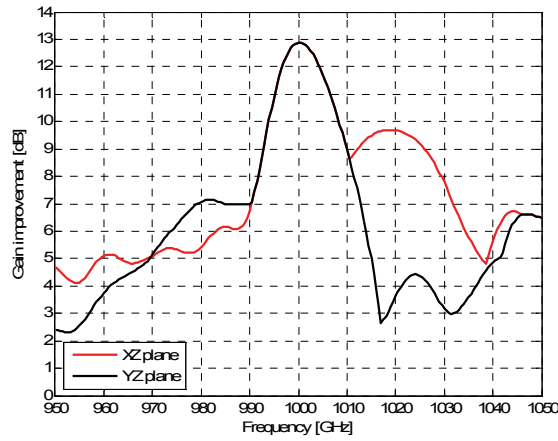


**Fig. 7.4:** Calculated gain improvement of the final antenna.

**Table 7.2:** Simulation results for basic antenna and final one.

| Results for $f=1$ THz, cavity = $\lambda/150$ | Basic antenna | Final antenna    |
|---|---------------|------------------|
| SSL, XZ plane                                 | -5.9 dB       | -22.0 dB         |
| SSL, YZ plane                                 | -5.5 dB       | -19.3 dB         |
| FBR, XZ plane                                 | 6.2 dB        | 22.0 dB          |
| FBR, YZ plane                                 | 5.5 dB        | 18.5 dB          |
| Main lobe width, XZ plane                     | 132.4°        | 33.8°            |
| Main lobe width, YZ plane                     | 136.1°        | 40.7°            |
| Gain, XZ plane                                | 4.6 dB        | 13.0 dB/14.8 dB* |
| Gain, YZ plane                                | 4.6 dB        | 13.0 dB/14.8 dB* |
| Gain improvement                              | 0.0 dB        | 8.4 dB/10.2 dB*  |
| Axial ratio                                   | 2.0 %         | 1.4 %            |
| Radiation efficiency                          | 57.5 %**      | 50.7 %**         |

(\*) Theoretical value calculated from complex reflection coefficient, (\*\*) Calculated by CST MWS for a conventional antenna without optical conversion.

## 7.2 Fabrication and technology aspects

THz photoconductive antennas belong to most common devices for the generation and detection of THz waves. A low efficiency is the major problem of this type of antennas. Thus, obtaining a high THz power is difficult.

Research of photoconductive antennas has started in early 1980s. Since then, many photoconductive antennas have been developed. Nevertheless, the antennas exploit the same principle of operation, which is quite different from conventional RF/microwave antennas.

A comparison of major differences between photoconductive and RF/microwave antennas is given in Table 7.3 [58].

**Table 7.3:** Comparison of RF/microwave antennas and photoconductive ones.

| Parameters            | Microwaves antennas                              | Photoconductive Antennas                          |
|-----------------------|--|---|
| Feed-line/source      | Transmission line                                | Laser beam  |
| Substrate             | Dielectric material with thickness $\ll \lambda$ | Material with thickness comparable with $\lambda$ |
| Bias voltage          | No   | Yes   |
| Impedance matching    | Easy to achieve                                  | Hard to achieve                                   |
| Manufacture           | Easy to make                                     | Hard to make                                      |
| Computer aided design | Available  | Not available                                     |

- Feed-line/source [58]:

For conventional antennas, various feed lines can be used (microstrip, CPW, etc.). For photoconductive antennas, no feed line exists in reality. Development of low loss THz transmission lines is very challenging [59]. Actually, laser is the feed line for photoconductive antennas.

- Substrate [58]:

As a substrate for conventional antennas, a low-loss dielectric material is used. As a substrate for THz antennas, we use photoconductive materials which are basically semiconductors (Si, InAs, ZnTe, GaSe, InP, SOS, GaAs, and InGaAs). Low-temperature-grown GaAs (LT-GaAs) has become the most popular material because of short photo-carrier lifetime (about 0.25 ps), high electric breakdown field ( $> 5 \cdot 10^5$  V/cm) and high mobility ( $> 200$  cm<sup>2</sup>/Vs). The thickness of the substrate of photoconductive antennas has to be comparable with the THz wavelength. Otherwise, unwanted substrate modes can be excited.

- Bias voltage [58]:

Whereas conventional antennas do not require a bias voltage, photoconductive antennas when used like transmitting ones require that.

- Impedance matching [58]:

Since no transmission lines are available for photoconductive antenna, no tuning circuit can ensure the impedance matching. The impedance matching is a big issue for photoconductive antennas.

- Manufacturing [58]:

THz antennas are usually fabricated by a conventional lithography on low temperature GaAs grown at about 250°C and post annealed at a higher temperature (but < 600 °C). The metal patterns are deposited using one of the usual schemes for ohmic contact on n-type GaAs.

- Computer aided design [58]:

There are no complete design tools available for the design of photoconductive antennas. These antennas are mainly developed by trial-and-error. Only metallic structures may be simulated using electromagnetic (EM) simulation tools.

In this work, we have chosen:

- Source: Dual-slot antenna with impedance matching [27];
- Substrate: LT-GaAs for source and GaAs for other layers;
- Bias voltage: Bias voltage was implemented by an RF choke filter;
- Computer design: CST MWS was used.

Discussion with supervisors resulted to the decision, that the final structure will be validated at the frequency  $f = 10$  GHz due to high costs of manufacturing.

### 7.3 Experimental verification at $f = 10$ GHz

The final antenna consists of the LC superstrate, mushroom-like EBG ground plane and CP cross-slot patch antenna. The feeding was implemented by microstrip transmission line. Structure of the antenna is shown in Fig. 7.5.

The square patch of a side length  $L_P = 6.17$  mm with metallization  $t = 0.035$  mm is etched on a substrate with the thickness  $h_2 = 0.762$  mm and the relative permittivity  $\epsilon_{r2} = 3.38$ . The microstrip feeding line is of characteristic impedance  $Z_0 = 50 \Omega$ . The matching line  $L_{OS} = 1.40$  mm is etched on a substrate with the thickness  $h_1 = 1.016$  mm and the relative permittivity  $\epsilon_{r1} = 10.2$ . The patch is excited via the cross-slot aperture. Lengths of arms of the cross are  $L_{S1} = 4.06$  mm and  $L_{S2} = 3.66$  mm. The center of the cross and the center of the patch have identical coordinates.

The dimensions of the mushroom-like EBG are periodicity  $D_{EBG} = 4.63$  mm, the width of the patch  $P_{EBG} = 4.33$  mm and the radius of via  $R_{EBG} = 0.6$  mm.

Fig. 7.6 shows frequency response of the reflection phase of the mushroom-like EBG and surface wave transmission of the mushroom-like EBG computed by CST MWS (the EBG has a positive reflection phase  $\phi_2 = 136.96^\circ$ ).

Fig. 7.7 shows the dispersion diagram of EBG. The band-gap is from 9.23 GHz to 10.70 GHz. Operating frequency is  $f = 10$  GHz. The EBG consists of  $17 \times 17$  unit cells.

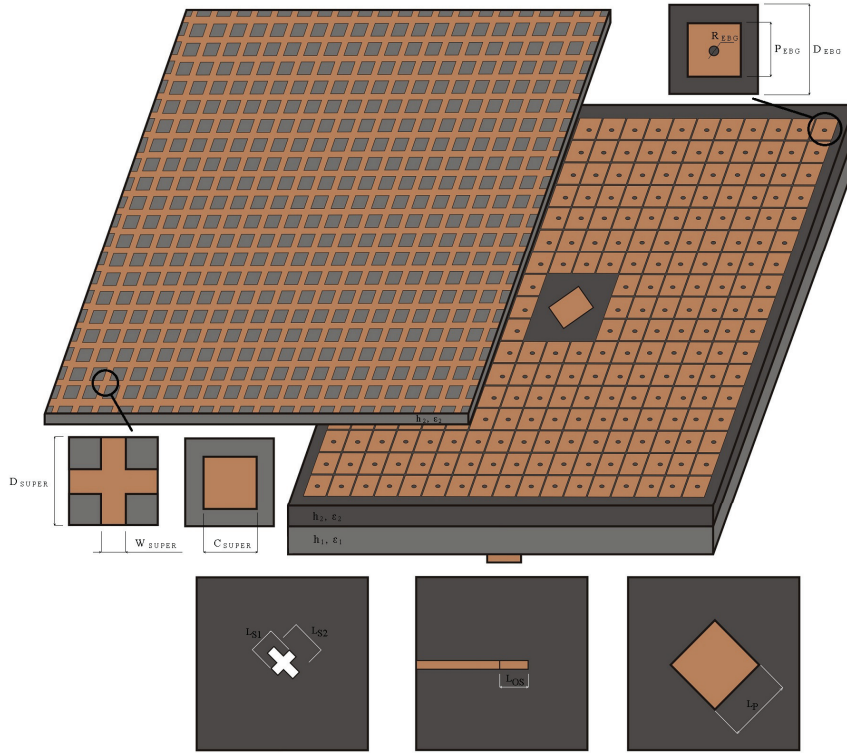


Fig. 7.5: Geometry of the final structure.

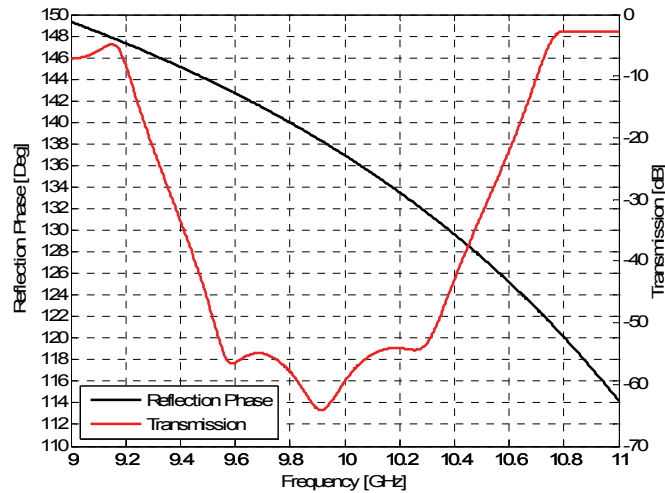


Fig. 7.6: Frequency response of reflection phase and surface wave transmission of the mushroom-like EBG structure.

The LC superstrate (double inductive and capacitive grid) allows us to obtain a phase shift of the reflection coefficient from  $+180^\circ$  to  $-180^\circ$ . The superstrate is made from the substrate with  $h_1 = 1.016$  mm and  $\epsilon_{r1} = 10.2$ . The capacitive metallic square patch is milled on one face and an inductive metallic mesh on another face of the substrate. The width of the inductive grid is  $W_{\text{super}} = 1.31$  mm, and the width of the capacitive patch is  $C_{\text{super}} = 3.19$  mm, both having a periodicity  $D_{\text{super}} = 3.19$  mm.

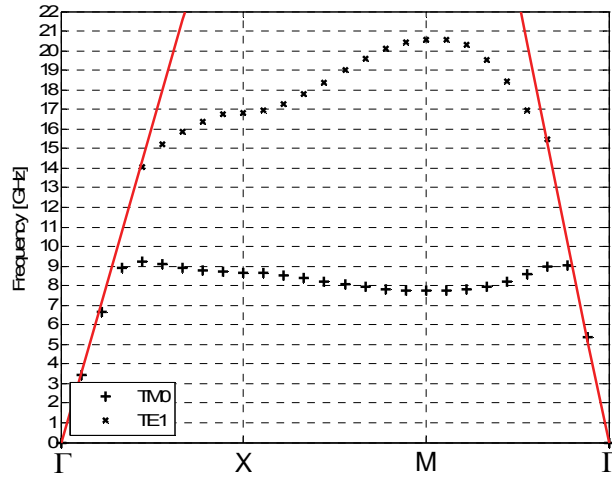


Fig. 7.7: Dispersion diagram of the mushroom-like EBG structure.

Figure 7.8 shows the reflection phase the magnitude of the LC superstrate. The LC superstrate has a negative reflection phase  $\phi_1 = -94.35^\circ$  and a high reflection coefficient 0.938 at the operating frequency. Using (6.11), we obtain a maximal gain  $G = 14.95$  dB. The superstrate creates the resonant cavity of the height  $h_{cavity} = 1.5$  mm ( $\lambda/22$ ). The LC superstrate consisted of  $21 \times 21$  unit cells. After optimization, the height of the cavity has changed to  $h_{cavity} = 1.35$  mm.

However, LC superstrate can be used with the reflection phase  $\phi_1 = -134.56$  to obtain the cavity height  $h_{cavity} = 0.1$  mm ( $\lambda/300$ ) with the maximal gain  $G = 19.95$  dB. Dimensions are  $W_{super} = 1.33$  mm,  $C_{super} = 3.43$  mm,  $D_{super} = 3.94$  mm. We have chosen  $h_{cavity} = 1.35$  mm due to fabrication aspects.

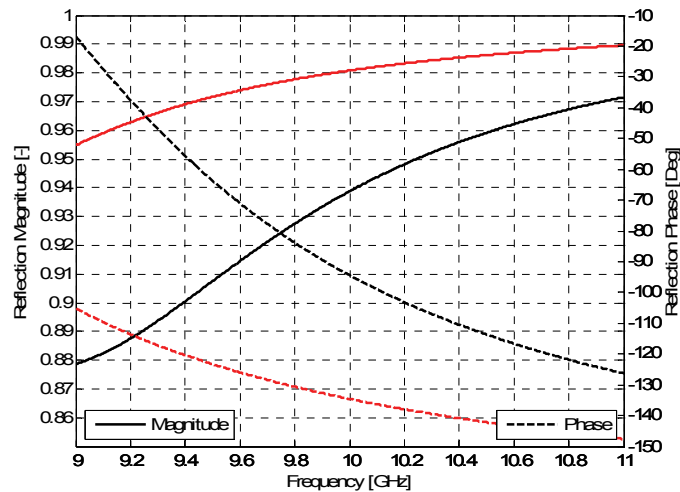
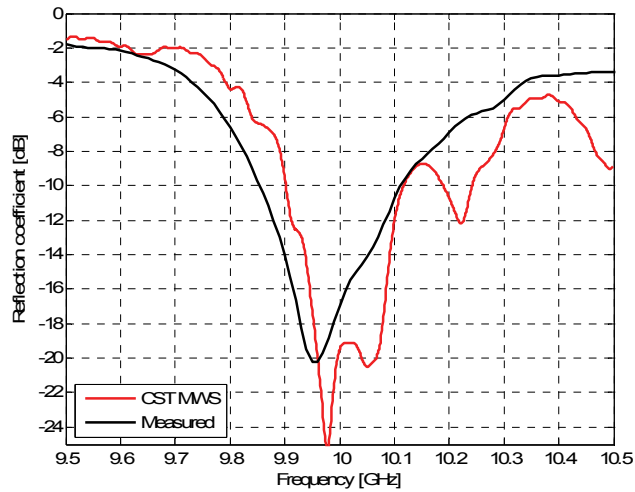


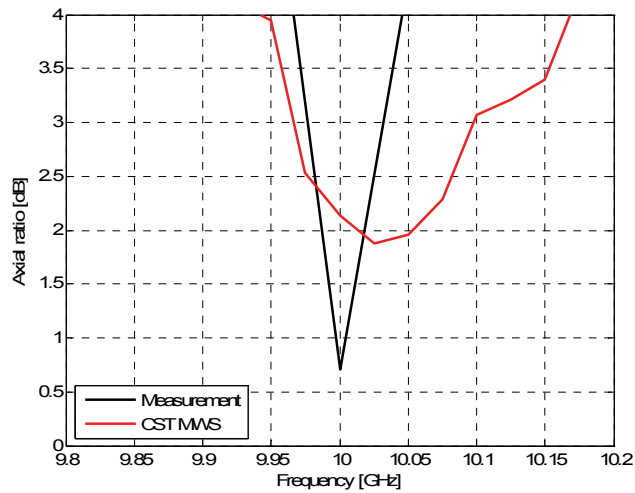
Fig. 7.8: Frequency response of reflection phase of the LC superstrate (black  $h = \lambda/22$ , red  $h = \lambda/300$ ).

In Figure 7.9, computed and measured frequency responses of reflection coefficient are compared. The impedance bandwidth of the measured antenna is 2.57%.



**Fig. 7.9:** Simulated and measured reflection coefficient of the final antenna.

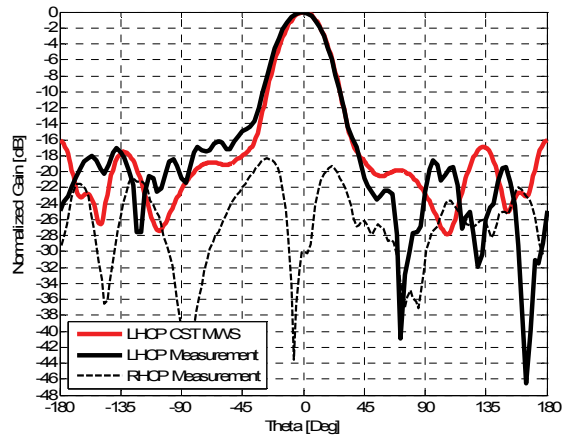
In Figure 7.10, computed and measured axial ratio in broadside direction is given. The axial ratio bandwidth is 0.6% against 1.9% achieved by CST MWS. Axial ratio strongly depends on the composition of each layer. In this case, the final antenna was set for generating the left-handed circular polarization (LHCP).



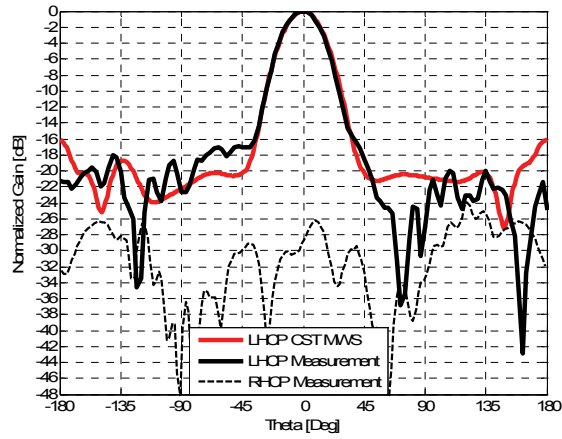
**Fig. 7.10:** Measured axial ratio of the final antenna.

Figure 7.11 shows simulated and measured radiation patterns at the center frequency.

Thanks to the band-gap, the mushroom-like EBG structure can suppress surface waves and reduce the side lobe level (Fig. 7.7). The results show smoother radiation patterns with smaller wasted power in the backward hemisphere. The comparison of the basic CP antenna (without EBG and superstrate, ground plane dimensions 83 mm × 83 mm) with the final simulated structure and measurements are shown in Table 7.4.



a)



b)

**Fig. 7.11:** Radiation patterns of fabricated antenna at 10 GHz a) XZ plane, b) YZ plane.

**Table.7.4:** Simulation and measurement results for final antenna.

| Results for $f = 10$ GHz  | Basic    | Final: Simulation | Final: Measurement |
|---------------------------|----------|-------------------|--------------------|
| SSL, XZ plane             | -11.9 dB | -21.7 dB          | -18.7 dB           |
| SSL, YZ plane             | -12.4 dB | -20.8 dB          | -18.5 dB           |
| FBR, XZ plane             | 13.6 dB  | 29.3 dB           | 24.2 dB            |
| FBR, YZ plane             | 13.6 dB  | 29.3 dB           | 21.2 dB            |
| $S_{11}$ bandwidth        | 4.0%     | 2.1 %             | 2.6 %              |
| AR bandwidth (3 dB)       | 2.1 %    | 1.9 %             | 0.6 %              |
| Cavity height             | none     | $\lambda/22$      | $\lambda/22$       |
| Main lobe width, XZ plane | 110.2°   | 25.6°             | 14.6°              |
| Main lobe width, YZ plane | 117.0°   | 26.6°             | 14.6°              |
| Gain, XZ plane            | 5.3 dB   | 16.0 dB           | 16.0 dB            |
| Gain, YZ plane            | 5.3 dB   | 16.0 dB           | 16.0 dB            |
| Gain improvement          | 0.0 dB   | 10.7 dB           | 10.7 dB            |

## 8 CONCLUSION

The thesis was focused on the design and modelling of circularly polarized THz antenna with circular polarization. The thesis contributed to the solution of following problems:

- We developed a technique for calculating the parasitic capacitance of the photoconductive mixer which respects the geometry of electrodes and the substrate.
- We designed a dual-slot antenna and a four-leaf-clover-shaped dipole. The four-leaf-clover-shaped dipole exhibited very high input impedance, which is suitable for the connection to the LT-GaAs photomixer.
- We designed a planar lens to focus the radiated energy into the main lobe and suppress the level of side lobes.
- We completed the final prototype of the circularly polarized antenna and verified its functionality by simulations and measurements.

The numerical results are summarized in the following table:

| <b>Dual-slot antenna (like THz source)</b> | <b>Value</b> |
|--|--------------|
| Main lobe magnitude                        | 9.1 dB       |
| Side lobe level, XZ Plane                  | -10.6 dB     |
| Side lobe level, YZ Plane                  | -12.8 dB     |
| Angular width (3 dB), XZ Plane             | 62.4°        |
| Angular width (3 dB), YZ Plane             | 34.8°        |
| Radiation efficiency                       | 61.4 %       |
| <b>Four-leaf-clover-shaped dipole</b>      | <b>Value</b> |
| Main lobe magnitude                        | 10.0 dB      |
| Side lobe level, XZ Plane                  | -7.6 dB      |
| Side lobe level, YZ Plane                  | -5.1 dB      |
| Angular width (3 dB), XZ Plane             | 44.2°        |
| Angular width (3 dB), YZ Plane             | 42.3°        |
| Radiation efficiency                       | 91.9 %       |
| <b>CP THz antenna with THz source</b>      | <b>Value</b> |
| Main lobe magnitude                        | 4.6 dB       |
| Side lobe level, XZ Plane                  | -5.9 dB      |
| Side lobe level, YZ Plane                  | -5.5 dB      |
| Angular width (3 dB), XZ Plane             | 132.4°       |
| Angular width (3 dB), YZ Plane             | 136.1°       |
| Radiation efficiency                       | 77.7 %       |

Second, the effort was aimed to exploit periodic structures for the implementation of a planar lens and an electromagnetic band gap substrate:

- We developed a method for correct design of periodic structures. We dealt with a mushroom-like EBG structure: the design method was developed, and experiment confirmed results. Surface waves were suppressed and antenna parameters were improved.
- We created two types planar lenses: (1) a conventional superstrate and (2) a novel LC superstrate. The LC superstrate allows the reduction of the height of the resonant cavity at minimum.

The numerical results are summarized in the following table:

| Results for $f = 1$ THz   | Simple antenna | Antenna with superstrate | Antenna with LC superstrate |
|---------------------------|----------------|--------------------------|-----------------------------|
| SSL, XZ plane             | -1.3 dB        | -14.7 dB                 | -22.0 dB                    |
| SSL, YZ plane             | -5.6 dB        | -10.4 dB                 | -19.3 dB                    |
| FBR, XZ plane             | 7.0 dB         | 14.7 dB                  | 22.0 dB                     |
| FBR, YZ plane             | 7.0 dB         | 14.7 dB                  | 18.5 dB                     |
| Main lobe width, XZ plane | 162.2°         | 14.6°                    | 33.8°                       |
| Main lobe width, YZ plane | 43.9°          | 14.6°                    | 40.7°                       |
| Gain, XZ plane            | 5.4 dB         | 18.7 dB                  | 13.0 dB                     |
| Gain, YZ plane            | 1.2 dB         | 18.7 dB                  | 13.0 dB                     |
| Gain improvement          | 0.0 dB         | 13.3 dB                  | 7.6 dB                      |
| Cavity height             | none           | $\lambda/2$              | $\lambda/150$               |

Finally, we experimentally verified described principles at 10 GHz. The designed structure affirmed the correctness of the concept and improvement of antenna parameters.

Now I would like to compare the advantages and disadvantages of my design with a conventional concept.

My design (advantages):

Circular polarization, small dimensions, planar structure, single superstrate for antenna matrix, small mutual coupling between antenna elements, side lobe level suppression, improvement of front to back ratio.

My design (disadvantages):

Complicated design, radiation efficiency, narrowband structure, losses in high permittivity dielectrics, skin effect.

Conventional concept (advantages):

Wideband and narrowband structures, high gain (directivity), easy to fabricate.

Conventional concept (disadvantages):

Large dimensions, each antenna element needs a silicon lens, intricately connection between the antenna and lens.

## REFERENCES

- [1] SIEGEL, P. Terahertz technology. *IEEE Transactions on Microwave Theory and Techniques*. 2002, vol. 50, no. 3, page 910 - 928.
- [2] EICHHORN, F. *Ultrabroadband Photonic Receiver Concepts for Terahertz Frequencies*. Master's thesis, Denmark: Technical University of Denmark, 2006.
- [3] CROWE, T., BISHOP, W., PORTERFIELD, D., HESLER, J., WEIKLE, R. M. Opening the terahertz window with integrated diode circuits. *IEEE Journal of Solid-State Circuits*. 2005, vol. 40, no. 10, page 2104 - 2110.
- [4] LOATA, G. *Investigation of low-temperature-grown GaAs photoconductive antennae for continuous-wave and pulsed terahertz generation*. Dissertation thesis, Germany: Vorgelegt beim Fachbereich Physik der Johann Wolfgang Goethe-Universität in Frankfurt am Main, 2007.
- [5] BROWN, E. R., WILD, W., CUNNINGHAM, C. Alma The Atacama Large Millimeter Array. *Advances in Space Research*. 2004, vol. 34, no. 3, page 555 - 559.
- [6] PHILLIPS, T., KEENE, J. Submillimeter Astronomy Heterodyne Spectroscopy. In *Proceedings of the IEEE*. 1992, vol. 80, no. 11, page 1662 - 1678.
- [7] LOER, T., SIEBERTT, K. J., HASAGAWA, N., HAHN, T., LOATA, G., WIPF, R., KRESS, M., THOMSON, M., ROSKOS, H. G. Terahertz Surface and Interface Characterization. *IEEE MTT-S International Microwave Symposium Digest*. 2005, pages 4.
- [8] FERGUSON, B., WANG, S., GRAY, D., ABBOTT, D., ZHANG, X-C. Towards Functional 3D T-ray Imaging. *Physics in Medicine and Biology*. 2002, vol. 47, page 3735 - 3742.
- [9] WALLACE, V. P., PICKWELL, E., FITZGERALD, A. J., PINDER, S. Terahertz Pulsed Imaging and Spectroscopy of Breast Tumours. *14th International Conference on Terahertz Electronics and Infrared Millimeter Waves*. 2006, page 585 - 585.
- [10] TRIBE, W. R., NENHAM, P. A., TADAY P. F., KEMP, M. C. Hidden Object Detection: Security Applications of Terahertz Technology. *Proceedings of Terahertz and Gigahertz Electronics and Photonics*. 2004 vol. 53, no. 54, page 168 - 176.
- [11] LEAHY-HOPPA, M. R., FITCH, M. J., ZHENG, X., HAYDEN, L. M., OSIANDER, R. Wideband Terahertz Spectroscopy of Explosives. *Chemical Physics Letters*. 2007 no. 434, vol. 50, page 227 - 230.
- [12] SYDLO, C., SIGMUND, J., FEIGIMOV, M., MEISSNER, P. HARTNAGEL, H. L. Coherent Generation and Detection of Continuous THz Waves Using Two Photomixers Driven by Laser Diodes. *Conference Digest of the 2004 Joint 29th International Conference on Infrared and Millimeter Waves and 12th International Conference on Terahertz Electronics*. 2004, page 200 - 201.
- [13] SASAKI, Y., SUIZU, K., ITO, H. Surface-emitted Terahertz-wave Generation Using Double Injection Seeded Optical Parametric Generation. *The 5th Pacific Rim Conference on Lasers and Electro-Optics*, 2003.
- [14] BROWN, E. R. THz Photomixing. *The 20th Annual Meeting of the IEEE Lasers and Electro-Optics Societ.*, 2007, page 790 - 791.

- [15] BROWN, E. R. Thz Generation by Photomixing in Ultrafast Photoconductors. *International Journal of High Speed Electronics and System*. 2003, vol. 13, no. 2, page 497 - 545.
- [16] FRITSCHÉ C. *Design and Modeling of an Ultrafast Broadband Photonic Mixer*. Master's thesis, Denmark: Technical University of Denmark, 2005.
- [17] RENNER, F., ECKARDT M., SCHWANHAUSSER, A., KLAR, O., MALZER., S., DOHLER, G., LOATA, G., LOFFLER, T., ROSKOS, H., HANSON, M., DRISROLL, D, GOSSARD, A. Thz-emitter Based on Ballistic Transport in nano-pin Diodes. *Physica Status Solidi (A) Applied Research*. 2005, page 965 - 969.
- [18] ITO, H., KODAMA, S., MURAMOTO, Y., FURUTA. T., NAGATSUMA, T., ISHIBASHI, T. High-speed and high-output in-p-ingaas Unitraveling-carrier Photodiodes. *IEEE Journal of Selected Topics in Quantum Electronics*. 2004, vol. 10, no. 4, page 709 - 727.
- [19] FRITSCHÉ, C., KROZER, V. Large-signal Pin Diode Model for Ultra-fast Photodetectors. *35th European Microwave Conference - Paris*. 2005.
- [20] ZEDLER, M., HARING-BOLIVAR, P., KURZ, H. Improved coherent THz emission by modification of the dielectric environment. *Quantum Electronics and Laser Science*, 2003.
- [21] DOWN, A., WHITTAKER, D. M., CORCHIA, A., DAVIES, A.G., LINFIELD, E.H. Enhancement of THz emission from semiconductor surfaces. *Tenth International Conference on Terahertz Electronics Proceedings*. 2002, page 48 - 51.
- [22] ITO, H., FURUTA, T., NAKAJIMA, F., YOSHINO, K., ISHIBASH, T. Photonic Generation of Continuous THz Wave Using Uni-Traveling-Carrier Photodiode. *Lightwave Technology*. 2005, vol. 23 , no. 12, page 4016 - 4021.
- [23] ITO, H., ISHIBASH, T. Ultrafast Uni-Traveling Carrier Photodiode. *58th Conference Device Research Conferenc*. 2000, page 165 - 168.
- [24] STUZTAN, W. L., THIELE G. A. *Antenna Theory and Design*, John Willey & Sons, 1998. ISBN-13: 978-0470576649.
- [25] MILLIGAN, T. A. *Modern Antenna Design*. New Jersey: John Willey & Sons, 2005. ISBN-13: 978-0471457763.
- [26] MENDIS, R., SYDLO, C., SIGMUND, J., FEIGINOV, M., MEISSNER, P., HARTNAGEL, H. L. Spectral Characterization of Broadband Thz Antennas by Photoconductive Mixing: Toward Optimal Antenna Design. *IEEE Antennas and Wireless Propagation Letters*. 2005, vol. 4, no. 1, page 85 - 88.
- [27] KAZIM, M. I. *Design of Continuous-Wave Photonic TeraHertz*. Antennas Master's thesis, Denmmar: Technical University of Denmark, 2006.
- [28] NGUYEN, T.K.,WOO, I., HAN, H., PARK, I., LIM, H. Four-leaf clover-shaped antenna on an extended hemispherical lens for a high-output-power THz photomixer. *35th International Conference on Infrared Millimeter and Terahertz Waves (IRMMW-THz)*, 2010.
- [29] PITRA, K.; RAIDÁ, Z.; HARTNAGEL, H. Design of Circularly Polarized Terahertz Antenna with Interdigital Electrode Photomixer. *In Proceedings of the European Conference on Antennas and Propagation, EuCAP 2013*. Gothenborg, Sweden: 2013. s. 2367-2370. ISBN: 978-88-907018-1- 8.

- [30] KAZIM, M. I., JEPSEN, P., KROZER, V. Design of THz Antennas for a Continuous-Wave Interdigitated Electrode Photomixer. *3rd European Conference on Antennas and Propagation (EUCAP). 2009*, page 1640 - 1644.
- [31] SYDLO C. *Reliability investigations and development of compound semiconductor devices for microwave and terahertz applications. Ph.D Thesis*, TU Darmstadt, Shaker, 2006. ISBN-10: 3832254005.
- [32] AJAYAN, K. R., VINOY, K. J. Planar Inter Digital Capacitors on Printed Circuit Board. *IEEE Trans. Microw. Theory Tech.* 1993, vol. 41, no. 9, page 191 - 194.
- [33] JUUL, L., MIKULICS, M., MARSO, M. Improving output power of terahertz heterodyne photomixer by impedance matching *International Conference on Advanced Semiconductor Devices & Microsystems (ASDAM)*, 2012, page 75 - 78.
- [34] HONG, J.S. *Microstrip Filters for RF/Microwave Applications*. New Jersey: John Wiley & Sons, Inc. 2001, ISBN: 978-0-470-40877-3.
- [35] SOKOL, V. Efficient Simulation of Electrically Large Structures, CST workshop 2010.
- [36] WOO, I., NGUYEN T.K., HAN, H., LIM, H., PARK, I. Four-leaf-clover-shaped antenna for a THz photomixer, *Optics Express*, Vol. 18, Issue 18, 2010 page 18532-18542.
- [37] PITRA, K.; KOVACS, P.; RAIDA, Z.; HARTNAGEL, H. Design of Circularly Polarized Terahertz Antenna with Superstrate (Cover) Layer. *In Proceedings of the International Conference on Electromagnetics in Advanced Applications (ICEAA)*. 15. Torino, Italy, 2013. page 363-363.
- [38] POZAR D.M, *Microwave Engineering*, Third Edition. John Wiley & Sons, Inc., 2005.
- [39] DEB, A., ROY, J.S., GUPTA, B. Design of Cross-slot Coupled Microstrip Antenna Using Self Adaptive Differential Evolution, *IEEE Applied Electromagnetics Conference (AEMC)*, 2011, page 1 - 4.
- [40] GARG, R., BHARTIA, P., BAHL, I., ITTIPIBOOM, A. *Microstrip Antenna Design Handbook*, Artech House, London, 2001.
- [41] SIEVENPIPER, D., ZHANG, L., BROAS, R. F. J., ALEXOPOULOS, N. G., YABLONOVITCH, E. High-impedance electromagnetic surfaces with a forbidden frequency band. *IEEE Transaction on Microwave Theory and Techniques*, vol. 47, issue 11, p. 2059-2074, 1999.
- [42] SIEVENPIPER, D. F. High-Impedance Electromagnetic Surfaces. *Ph.D Thesis*, University of California (UCLA) Los Angeles, CA, 1999.
- [43] KERN, D. J., WERNER, D. H., MONORCHIO, A., LANUZZA, L., WILHELM, M. J. The Design Synthesis of Multiband Artificial Magnetic Conductors Using High Impedance Frequency Selective Surfaces. *IEEE Transaction on Antennas and Propagation*, vol. 53, issue 1, p. 8 – 17., 2005.
- [44] KOVACS, P. Design and optimization of electromagnetic band gap structures. *Ph.D Thesis*, Brno University of Technology, Brno, 2010.
- [45] TRETYAKOV, S. *Analytical Modeling in Applied Electromagnetics*. Artech House, 2003
- [46] MONORCHIO, A., GENOVESI, S., SERRA, U., MANARA, G., Optimal design of artificial magnetic conductors including angular response. *IEEE Antennas and Propagation Society International Symposium*, 2006.
- [47] SANADA, A. *Planar single and double negative material implementations and applications*. URSI, 2005.

- [48] COLLIN, R. *Field Theory of Guided Waves (2nd edition)*. IEEE Press, New York, 1991.
- [49] NGUYEN, T.T, KIM, D.J, KIM, S.H., JANG, J.H. Design of a Wideband Mushroom-like Electromagnetic Bandgap Structure with Magneto-Dielectric Substrate. The 6th International Conference on Information Technology and Applications (ICITA 2009), page 6.
- [50] YANAGI, T., OSHIMA, T., OH-HASHI, H., KONISHI, Y., MURAKAMI, S., ITOH, K., SANADA, A. Lumped-Element Loaded EBG Structure with an Enhanced Bandgap and Homogeneity. *International Workshop on Antenna Technology: Small Antennas and Novel Metamaterials, 2008*. page 458 - 461
- [51] ILUZ, Z., SHAVIT, R., BAUER, R. Microstrip antenna phased array with electromagnetic bandgap substrate. *IEEE Transactions on Antennas and Propagation*, 2004, vol. 52, no. 6, p. 1446 - 1453.
- [52] KOVÁCS, P., URBANEC, T. Electromagnetic Band Gap Structures: Practical Tips and Advice for Antenna Engineers. *Radioengineering*, 2012, roč. 21, č. 1, s. 414-421. ISSN: 1210 - 2512.
- [53] FERESIDIS, A., P., GOUSETTIS, G., WANG, S., VARDAXOGLU, C, J. Artificial Magnetic Conductor Surfaces and Their Application to Low-Profile High-Gain Planar Antennas. *IEEE Transactions on Antennas and Propagation*, January, 2005, vol. 53, page 209 – 215.
- [54] PALIKARAS, G. K., FERESIDIS, A. P., VARDAXOGLU, J. C. Cylindrical electromagnetic bandgap structures for directive base station antennas, *IEEE Antennas Wireless Propag. Lett.* , vol. 3, 2004. page 87 – 89,
- [55] BOUTAYEB, H., MAHDJOUBI, K., TAROT, A.C., DENIDNI, T.A. Directivity of an antenna embedded inside a Fabry-Perot cavity: Analysis and design, *Microwave Opt Technol Lett 48* (2006), page 12 - 17.
- [56] LI, Y., ESSELLE, K.P. Small EBG resonator high-gain antenna using in-phase highly-reflecting surface, *Electron Lett 45*, 2009. page 1058–1060.
- [57] OURIR, A., DE LUSTRAC, A., LOURTIOZ, J.M. Optimization of metamaterial based subwavelength cavities for ultracompact directive antennas, *Microwave Opt Technol Lett 48*, 2006, page 2573 – 2577.
- [58] HUANG, Y., KHIABANI, N., SHEN. Y., LI, D. Terahertz Photoconductive Antenna Efficiency, *International Workshop on Antenna Technology (iWAT)*, 2011, page 152 - 156.
- [59] WANG, K., MITTLEMAN, D. M. Metal wires for terahertz waveguiding, *Nature, Vol. 432, 18 Nov. 2004*, page 376-379.

## CURRICULUM VITAE

**Name:** Kamil Pítra  
**Born:** April 2<sup>nd</sup> 1984 in Strakonice, Czech Republic  
**Contact:** kamil.pitra@seznam.cz

### Education:

2010 - 2014 Brno University of Technology /Department of Radio Electronics  
Doctoral's degree, Electronics and Communications  
Thesis: (Sub)millimeter-wave antennas

2008 - 2010 Brno University of Technology / Department of Radio Electronics  
Master's degree, Electronics and Communications  
Thesis: Antennas for millimeter-wave bands

2005 - 2008 Brno University of Technology /Department of Radio Electronics  
Bachelor's degree, Electronics and Communications  
Thesis: Low altitude FM radio-altimeter

### Experience:

10/2013 to 11/2013 TU Darmstadt (Prof. Hartnagel), Germany  
Study stay: Analysis and design of antennas for THz frequency band.

3/2013 to 5/2013 TU Darmstadt (Prof. Hartnagel), Germany  
Study stay: Analysis and design of antennas for THz frequency band.

11/2013 to 12/2011 TU Darmstadt (Prof. Hartnagel), Germany  
Study stay: Analysis and design of antennas for THz frequency band.

### Languages:

Czech, English

### Specialization:

Analysis and design of antennas, modelling and simulation of microwave and RF structures, antenna measurement

### **Selected Publications:**

PÍTRA, K.; RAIDA, Z. Planar Millimeter-Wave Antennas: A Comparative Study. *Radioengineering*, 2010, roč. 20, č. 1, s. 263-269. ISSN: 1210- 2512

PÍTRA, K.; RAIDA, Z.; BARTYZAL, J. Antenna Structures for Emerging Frequency Bands. In *18 telecommunications forum - TELFOR 2010*. 2010. s. 1-3. ISBN: 978-86-7466-392- 9.

PÍTRA, K.; RAIDA, Z. Wideband Feeders for Millimeter- Wave Horn Antennas. In *Proceeding of 15th Conference Microwaves Techniques COMITE 2010*. Brno: VUT BRNO, 2010. s. 39-41. ISBN: 978-1-4244-6351- 0.

PÍTRA, K. *Antennas for Millimeter- Wave Bands*. 21st International Travelling Summer School. 1. Darmstadt, Germany: Technische Universitat Darmstadt, 2011.

RAIDA, Z.; CIGÁNEK, J.; KADLEC, P.; KOUDELKA, V.; ŠEDĚNKA, V.; SVOBODOVÁ, J.; KOVÁCS, P.; LÁČÍK, J.; PÍTRA, K.; POKORNÝ, M.; PUSKELY, J.; VŠETULA, P.; WOLANSKÝ, D. *Mikrovlnné struktury z netradičních materiálů*. Odborné monografie. Odborné monografie. Brno: MJ Servis, 2011. 410 s. ISBN: 978-80-214-4419- 5.

PÍTRA, K.; RAIDA, Z. Small Antenna for Aerobatic Aircraft. In *Proceedings of the European Conference on Antennas and Propagation, EuCAP 2012*. Praha: 2012. s. 100-104. ISBN: 978-1-4577-0919- 7.

PÍTRA, K.; RAIDA, Z.; HARTNAGEL, H. Design of Circularly Polarized Terahertz Antenna with Interdigital Electrode Photomixer. In *Proceedings of the European Conference on Antennas and Propagation, EuCAP 2013*. Gothenborg, Sweden: 2013. s. 2367-2370. ISBN: 978-88-907018-1- 8.

PÍTRA, K.; RAIDA, Z. Miniaturized Antenna for Body Centric Communication. In *Proceedings of the European Conference on Antennas and Propagation, EuCAP 2013*. Gothenborg, Sweden: 2013. s. 3119-3122. ISBN: 978-88-907018-1- 8.

PÍTRA, K.; KOVÁCS, P.; RAIDA, Z.; HARTNAGEL, H. Design of Circularly Polarized Terahertz Antenna with Superstrate (Cover) Layer. In *Proceedings of the International Conference on Electromagnetics in Advanced Applications(ICEAA)*. 15. Torino, Italy: 2013. s. 363-363. ISBN: 978-1-4673-5705- 0.